Draft version April 29, 2022
Typeset using LaTeX **twocolumn** style in AASTeX63

Kepler and the Behemoth: Three Mini-Neptunes in a 40 Million Year Old Association

L. G. Bouma,[1,*] R. Kerr,[2] J. L. Curtis,[3] H. Isaacson,[4] L. A. Hillenbrand,[1] A. W. Howard,[1] A. L. Kraus,[2] A. Bieryla,[5] D. W. Latham,[5] E. A. Petigura,[6] and D. Huber[7]

[1]Cahill Center for Astrophysics, California Institute of Technology, Pasadena, CA 91125, USA
[2]Department of Astronomy, The University of Texas at Austin, Austin, TX 78712, USA
[3]Department of Astronomy, Columbia University, 550 West 120th Street, New York, NY 10027, USA
[4]Astronomy Department, University of California, Berkeley, CA 94720, USA
[5]Center for Astrophysics | Harvard & Smithsonian, 60 Garden St, Cambridge, MA 02138, USA
[6]Department of Physics & Astronomy, University of California Los Angeles, Los Angeles, CA 90095, USA
[7]Institute for Astronomy, University of Hawaii, 2680 Woodlawn Drive, Honolulu, HI 96822, USA

(Received —; Revised —; Accepted —)

ABSTRACT

Stellar positions and velocities from Gaia are yielding a new window on open cluster dispersal. Here we present an analysis of a group of stars spanning Cepheus ($l = 100°$) to Hercules ($l = 40°$), hereafter the Cep-Her complex. The group includes four Kepler Objects of Interest: Kepler-1643 b ($R_{\rm p} = 2.32 \pm 0.14\,R_\oplus$, $P = 5.3$ days), KOI-7368 b ($R_{\rm p} = 2.22 \pm 0.12\,R_\oplus$, $P = 6.8$ days), KOI-7913 Ab ($R_{\rm p} = 2.34 \pm 0.18\,R_\oplus$, $P = 24.2$ days), and Kepler-1627 Ab ($R_{\rm p} = 3.85 \pm 0.11\,R_\oplus$, $P = 7.2$ days). The latter Neptune-sized planet is in part of the Cep-Her complex called the δ Lyr cluster (Bouma et al. 2022). Here we focus on the former three systems, which are in other regions of the association. Based on kinematic evidence from Gaia, stellar rotation periods from TESS, and spectroscopy, these three objects are also ≈40 million years (Myr) old. More specifically, we find that Kepler-1643 is 46^{+9}_{-7} Myr old, based on its membership in a dense sub-cluster of the complex called RSG-5. KOI-7368 and KOI-7913 are 36^{+10}_{-8} Myr old, and are in a diffuse region that we call CH-2. Based on the transit shapes and high resolution imaging, all three objects are most likely planets, with false positive probabilities of 6×10^{-9}, 4×10^{-3}, and 1×10^{-4} for Kepler-1643, KOI-7368, and KOI-7913 respectively. These planets demonstrate that mini-Neptunes with sizes of ∼2 Earth radii exist at ages of 40 million years.

Keywords: exoplanet evolution (491), open star clusters (1160), stellar ages (1581)

1. INTRODUCTION

The discovery and characterization of planets younger than a billion years is a major frontier in current exoplanet research. The reason is that the properties of young planets provide benchmarks for studies of planetary evolution. For instance, young planets can inform our understanding of when hot Jupiters arrive on their close-in orbits (Dawson & Johnson 2018), how the sizes of planets with massive gaseous envelopes evolve (Rizzuto et al. 2020), the timescales for close-in multiplanet systems to fall out of resonance (Izidoro et al. 2017; Arevalo et al. 2022; Goldberg & Batygin 2022), and whether and how mass-loss explains the radius valley (Lopez et al. 2012; Owen & Wu 2013; Fulton et al. 2017; Ginzburg et al. 2018; Lee & Connors 2021).

The discovery of a young planet requires two claims to be true: the planet must exist, and its age must be secured. Spaced-based photometry from K2 and TESS has yielded a number of exemplars for which the planetary evidence comes from transits, and the age is based on either cluster membership (Mann et al. 2017; David et al. 2019; Newton et al. 2019; Bouma et al. 2020; Nardiello et al. 2020) or else on correlates of youth such as stellar rotation, photospheric lithium content, x-ray activity, and emission line strength (Zhou et al. 2021; Hedges et al. 2021).

In this work, we leverage recent analyses of the Gaia data, which have greatly expanded our knowledge of stellar groups (e.g., Cantat-Gaudin et al. 2018; Kounkel & Covey 2019; Kerr et al. 2021). To date these analyses have mostly clustered on stellar positions and 2D velocities. One important

Corresponding author: L. G. Bouma
luke@astro.caltech.edu

* 51 Pegasi b Fellow

result has been the discovery of diffuse streams and tidal tails comparable in stellar mass to the previously known cores of nearby open clusters (Meingast et al. 2019; Meingast et al. 2021; Gagné et al. 2021). Even though these streams are spread over tens to hundreds of parsecs, their velocity dispersions can remain coherent at the $\sim$1 km s^{-1} level. Internal dynamics and projection effects can also drive them to be much larger: in the Hyades, stars in the tidal tails are expected to span up to $\pm 40\,\mathrm{km\,s^{-1}}$ in velocity relative to the cluster center (Jerabkova et al. 2021). The stars in such diffuse regions can be verified to be the same age as the core cluster members through analyses of color–absolute magnitude diagrams (Kounkel & Covey 2019), stellar rotation periods (Curtis et al. 2019; Bouma et al. 2021), and chemical abundances (Hawkins et al. 2020). While there are implications for our understanding of star formation and cluster evolution (Dinnbier & Kroupa 2020), a separate consequence is that we now know the ages of many more stars, including previously known planet hosts.

The prime Kepler mission (Borucki et al. 2010) found most of the currently known transiting exoplanets, and it was conducted before Gaia. It is therefore sensible to revisit the Kepler field, given our new knowledge of the stellar ages.

Here, we expand on our earlier study of a 38^{+7}_{-6} Myr old Neptune-sized planet in the Kepler field (Kepler-1627 Ab; Bouma et al. 2022). This planet's age was derived based on its host star's membership in the δ Lyr cluster. While our analysis of the cluster focused on the immediate vicinity of Kepler-1627 in order to have a reasonable scope, it became clear that the δ Lyr cluster seems to also be part of a much larger group of similarly aged stars. This group, which is at a distance of $\sim$330 pc from the Sun, spans Cepheus to Hercules (galactic longitudes, l, between 40° and 100°), at galactic latitudes between 0° and 20°. We therefore refer to it as the Cep-Her complex. It exhibits significant sub-structure over its $\approx$250 parsec length, and a detailed analysis of its memberships, kinematics, and possible origin is currently being prepared as part of the 1 kpc expansion of the SPYGLASS project (R. Kerr et al. in prep).

Our focus is on the intersection of the Cep-Her complex with the Kepler field. Cross-matching our Cep-Her members against known Kepler Objects of Interest (KOIs; Thompson et al. 2018) yielded four candidate cluster members: Kepler-1627, Kepler-1643, KOI-7368, and KOI-7913. Given our earlier analysis of Kepler-1627, we focus here on the latter three objects. After analyzing the relevant properties of Cep-Her (Section 2), we derive the stellar properties (Section 3) and validate the planetary nature of each system using a combination of the Kepler photometry and high-resolution imaging (Section 4). We conclude with a discussion of mini-Neptune size evolution, and point out possible directions for future work (Section 5).

2. THE CEP-HER COMPLEX

2.1. *Previous Related Work*

Our focus is on a region of the Galaxy 200 to 500 pc from the Sun, above the galactic plane, and spanning galactic longitudes of 40° to 100°. Two rich clusters in this region are the δ Lyra cluster (Stephenson 1959) and RSG-5 (Röser et al. 2016). Each of these clusters was known before Gaia. Their reported ages are between 30 and 60 Myr. Early empirical evidence that these two clusters could be part of a large and more diffuse population was apparent in the Gaia-based photometric analysis of pre-main-sequence stars by Zari et al. (2018, see their Figures 11 and 13). Further kinematic connections and complexity were highlighted by Kounkel & Covey (2019), who included these previously known groups in the larger structures dubbed "Theia 73" and "Theia 96"[1]. The connection made by Kounkel & Covey (2019) between the previously known open clusters and the other groups in the region was made as part of an unsupervised clustering analysis of the Gaia DR2 positions and on-sky velocities with a subsequent manual "stitching" step. Their results support the idea that there is an overdensity of 30 to 60 Myr old stars in this region of the Galaxy. Kerr et al. (2021), in a volume-limited analysis of the Gaia DR2 point-source catalog out to one third of a kiloparsec, identified three of the nearest subpopulations, dubbed "Cepheus-Cygnus", "Lyra", and "Cerberus". Kerr et al. (2021) reported ages for each of these subgroups between 30 and 35 Myr.

2.2. *Member Selection*

The possibility that the δ Lyr cluster, RSG-5, and the subpopulations identified by Kerr et al. (2021) share a common origin has yet to be fully substantiated, but preliminary clustering results from the 1 kpc SPYGLASS analysis (R. Kerr et al. in prep) suggest the presence of contiguous stellar populations connecting each of these groups. In this work, our primary interest in the region stems from the fact that a portion of it was observed by Kepler (Figure 1, top panel). To further explore this sub-population, we select candidate Cep-Her members through four steps, the first three being identical to those described in Section 3 of Kerr et al. (2021). We briefly summarize them here.

The first step is to select stars that are photometrically distinct from the field star population based on Gaia EDR3 magnitudes $\{G, G_{\rm RP}, G_{\rm BP}\}$, parallaxes and auxiliary reddening estimates (Lallement et al. 2019). This step yielded 1,097 stars with high-quality photometry and astrometry. These stars are either pre-main-sequence K and M dwarfs due to their long contraction timescales, or massive stars near

[1] See their visualization online at http://mkounkel.com/mw3d/mw2d.html (accessed 15 March 2022)

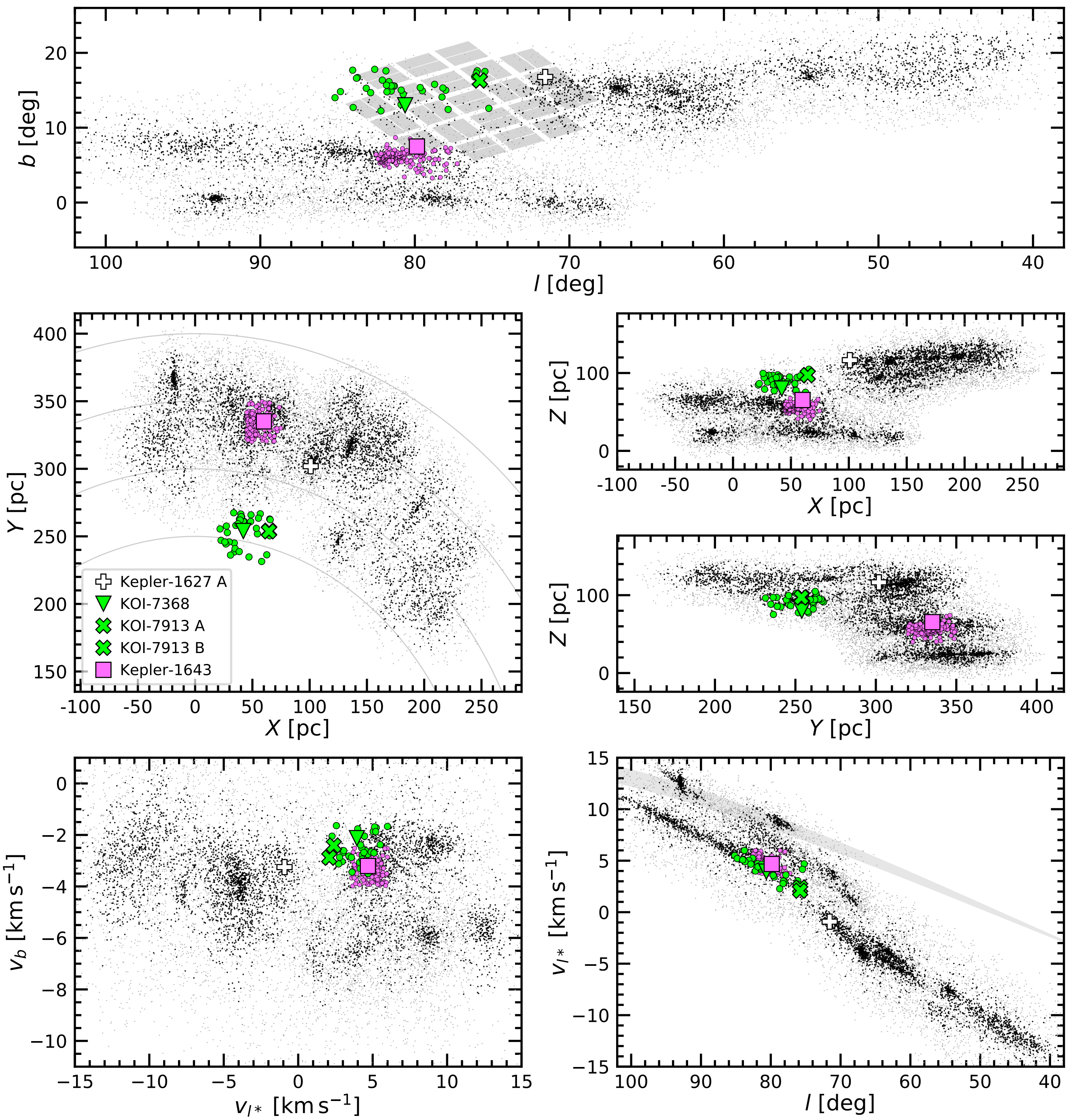

Figure 1. Positions and velocities of candidate members of the Cep-Her complex. *Top row*: On-sky positions in galactic coordinates. Black points are stars for which group membership is more secure than for gray points. Kepler-1627 is in the outskirts of the δ Lyr cluster (Bouma et al. 2022), which is centered at $(l, b) \approx (66^\circ, 12^\circ)$. The Kepler footprint is shown in gray. *Middle row*: Galactic positions. The Sun is at $(X, Y, Z) = (0, 0, 20.8)$ pc; lines of constant heliocentric distance are shown between 250 and 400 pc, spaced by 50 pc. *Bottom row*: Galactic tangential velocities (left) and galactic longitudinal velocity versus galactic longitude (right). The gray band in the lower-right shows the ± 1-σ projection of the Solar velocity with respect to the local standard of rest. There is a strong spatial and kinematic overlap between Kepler-1643 and RSG-5 (magenta). The local population of candidate young stars around KOI-7368 and KOI-7913 is more diffuse – we call this region "CH-2" (lime-green). The selection method for all of the stars displayed is described in Section 2.2.

the zero-age main sequence due to their rapid evolutionary timescales.

The second step is to perform an unsupervised HDBScan clustering on the photometrically selected population (Campello et al. 2015; McInnes et al. 2017). The parameters we use in the clustering are $\{X, Y, Z, cv_b, cv_{l^*}\}$, where c is the size-velocity corrective factor, which is taken as $c = 6\,\mathrm{pc}/\mathrm{km\,s^{-1}}$ to ensure that the spatial and velocity scales have identical standard deviations. Positions are computed assuming the `astropy v4.0` coordinate standard (Astropy Collaboration et al. 2018), which places the Sun 8122 pc from the galactic center, and assumes the solar velocity with respect to the local standard of rest from Schönrich et al. (2010). As input parameters to HDBScan, we set the minimum ϵ threshold past which clusters cannot be fragmented as 25 pc in physical space, and $25/c$ km s^{-1} in velocity. The minimum cluster size N is set to 10, as is k, the parameter used to define the "core distance" density metric.

This unsupervised clustering in this case yielded 8 distinct subgroups. These groups are then used as the "seed" populations for the third step, which is to search for objects at least as close to the 10$^{\mathrm{th}}$ nearest HDBScan-identified member in space-velocity coordinates. This third step yields stars that are spatially and kinematically close to the photometrically young stars, but which cannot be identified as young based on their positions in the color–absolute magnitude diagram.

The outcome of the analysis up to the point of the third step is shown in Figure 1. To enable a selection cut that filters out field-star contaminants, we also compute a weight metric, D, defined such that the group member with the smallest core distance has $D = 1$, the group member with the greatest core distance has $D = 0$, and weights for the other group members are log-normally distributed between these two extremes. After applying a set of quality cuts on the astrometry and photometry,[2] this procedure yields $D \sim \log_{10}\mathcal{N}(-1.55, 0.61)$. To visualize the results, in Figure 1 we show 12,436 objects with $D > 0.02$ as gray points, and 4,763 objects with $D > 0.10$ as black points. The previously known δ Lyr cluster is visible at $(l, b) = (68^\circ, 15^\circ)$ and $(v_{l'}, v_b) = (-4.5, -4)\,\mathrm{km\,s^{-1}}$. RSG-5 is visible at $(l, b) = (83^\circ, 6^\circ)$, $(v_{l'}, v_b) = (5.5, -3.5)\,\mathrm{km\,s^{-1}}$. Most of the other subclusters, including in Cep-Cyg $(l, b = 90^\circ, 7^\circ)$ and Cerberus $(l, b = 48^\circ, 18^\circ)$ are too small or dispersed to have previously been analyzed in great detail.

Our fourth and final step was to cross-match the candidate Cep-Her member list against all known Kepler Objects of Interest. We used the Cumulative KOI table from the NASA Exoplanet Archive from 27 March 2022, and also compared against the `q1_q17_dr25` table (Thompson et al. 2018). From the candidate members with weights exceeding 0.02, this yielded 11 known false positives, 6 "confirmed" planets, and 8 "candidate" planets. Inspection of the Kepler data validation summaries and Robovetter classifications for these objects showed whether they were potentially consistent with being *i)* planets, and *ii)* $\lesssim 10^8$ years old, based on the presence of rotational modulation at the expected period and amplitude (e.g., Rebull et al. 2020, Figure 9). Four objects remained after this inspection: Kepler-1627, Kepler-1643, KOI-7368, and KOI-7913.

Figure 1 shows the positions of the KOIs along various projections. Kepler-1643 is near the core RSG-5 population both spatially and kinematically. KOI-7368 and KOI-7913 are in a diffuse region ≈40 pc above RSG-5 in Z and ≈100 pc closer to the Sun in Y. In tangential galactic velocity space, there is some kinematic overlap between the region the latter two KOIs are in and the main RSG-5 group.

We define two sets of stars in the local vicinity of our objects of interest. For candidate RSG-5 members, we require:

$$\begin{aligned} X/\mathrm{pc} &\in [45, 75] \\ Y/\mathrm{pc} &\in [320, 350] \\ Z/\mathrm{pc} &\in [40, 80] \\ v_b/\mathrm{km\,s^{-1}} &\in [-4, -2.5] \\ v_{l^*}/\mathrm{km\,s^{-1}} &\in [3.5, 6], \end{aligned}$$

though the cluster does have a greater spatial extent toward smaller X (Figure 1, middle panels). For the diffuse stars near KOI-7368 and KOI-7913, we require

$$\begin{aligned} X/\mathrm{pc} &\in [20, 70] \\ Y/\mathrm{pc} &\in [230, 270] \\ Z/\mathrm{pc} &\in [75, 105] \\ v_b/\mathrm{km\,s^{-1}} &\in [-3.5, -1.5] \\ v_{l^*}/\mathrm{km\,s^{-1}} &\in [2, 6] \end{aligned}$$

and we call this latter set of stars "CH-2", using the preliminary Cep-Her (CH) subgroup identifier from R. Kerr et al. (in prep). These cuts yield 173 candidate RSG-5 members, and 37 candidate CH-2 members. These stars are listed in Appendix A, as are the Cep-Her candidates that were observed by Kepler, and all of our candidate matches against the Kepler Objects of Interest. An important consideration, especially for CH-2, is the contamination rate by field stars. We assess this in the following section.

2.3. *The Cluster's Age*

2.3.1. *Color–Absolute Magnitude Diagram*

Color–absolute magnitude diagrams (CAMDs) of the candidate RSG-5 and CH-2 members are shown in the upper row of Figure 2. The stars from the δ Lyr cluster are from Bouma

[2] $\varpi/\sigma_\varpi > 5$; $G/\sigma_G > 50$; $G_{\mathrm{RP}}/\sigma_{G_{RP}} > 20$; $G_{\mathrm{BP}}/\sigma_{G_{BP}} > 20$.

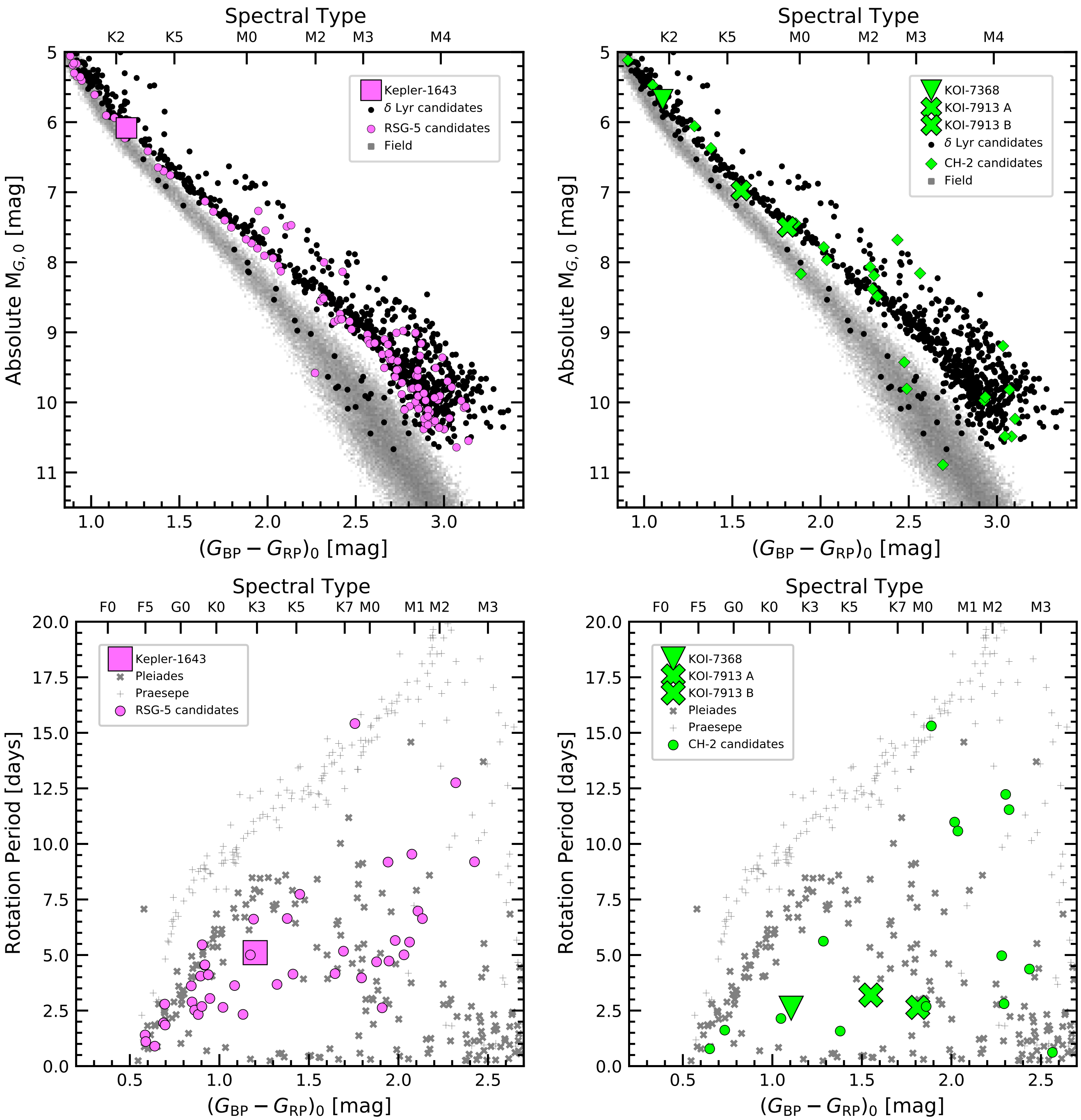

Figure 2. The stellar groups near KOI-7368, KOI-7913, and Kepler-1643 are 40 to 50 million years old. *Top row*: Color–absolute magnitude diagram of candidate Cep-Her members, plotted over candidate members of the δ Lyr cluster ($\approx$ 38 Myr; Bouma et al. 2022) and the Gaia EDR3 Catalog of Nearby Stars (gray background). The left and right columns shows stars in RSG-5 and CH-2, respectively. The range of colors is truncated to emphasize the pre-main-sequence. Stars that fall far below the cluster sequences are field interlopers. *Bottom row*: TESS and ZTF-derived stellar rotation periods, with the Pleiades ($\approx$ 112 Myr) and Praesepe ($\approx$ 650 Myr) shown for reference (Rebull et al. 2016; Douglas et al. 2017). The detection efficiency for reliable rotation periods falls off beyond $(G_{BP} - G_{RP})_0 \gtrsim 2.6$.

et al. (2022), and the field stars are from the Gaia EDR3 Catalog of Nearby Stars (Gaia Collaboration et al. 2021b). To make these diagrams, we imposed the data filtering criteria from Gaia Collaboration et al. (2018a, Appendix B), which include binaries while omitting artifacts from for instance low photometric signal to noise, or a small number of visibility periods. We then corrected for extinction using the Lallement et al. (2018) dust maps and the extinction coefficients $k_X \equiv A_X/A_0$ from Gaia Collaboration et al. (2018a), assuming that $A_0 = 3.1E(B-V)$. This yielded a mean and standard deviation for the reddening of $E(B-V) = 0.036 \pm 0.002$ for RSG-5, and $E(B-V) = 0.017 \pm 0.001$ for CH-2. By way of comparison, in Bouma et al. (2022) the same query for the δ Lyr cluster yielded $E(B-V) = 0.032 \pm 0.006$. Finally, for the plots we set the color range to best visualize the region of maximal age information content: the pre-main-sequence.

The CAMDs show that for RSG-5, all but one of the candidate members are on a tight pre-main-sequence locus. This implies a false positive rate of a few percent, at most. By comparison, our control sample (the δ Lyr candidates) has a false positive rate of $\approx$12%, based on the number of stars that photometrically overlap with the field population, while being outliers from the bulk cluster population. For CH-2, our membership selection gives 27 objects in the color range displayed, and 23 of them appear to be consistent with being on the pre-main-sequence. This implies a false positive rate in CH-2 of $\approx$15%.

Figure 2 also shows that most RSG-5 and CH-2 members overlap with the δ Lyr cluster, and that the groups are therefore roughly the same age. To quantify this, we use the method introduced by Gagné et al. (2020, their Section 6.3). The idea is to fit the pre-main-sequence loci of a set of reference clusters, and to then model the locus of the target cluster as a linear combination of these reference cluster loci. For our reference clusters, we used UCL, IC 2602, and the Pleiades, with the memberships reported by Damiani et al. (2019) and Cantat-Gaudin et al. (2018) respectively. We adopted ages of 16 Myr for UCL (Pecaut & Mamajek 2016), 38 Myr for IC 2602 (David & Hillenbrand 2015; Randich et al. 2018) and 112 Myr for the Pleiades (Dahm 2015). These assumptions and the subsequent processing steps taken to exclude field stars and binaries were identical to those described in Bouma et al. (2022). The mean and uncertainty of the resulting age posterior are 46^{+9}_{-7} Myr for RSG-5, and 36^{+10}_{-8} Myr for CH-2. For comparison, this procedure yields an age for the δ Lyr cluster of 38^{+6}_{-5} Myr. The older isochronal age of RSG-5 is consistent with its location relative to the δ Lyr cluster in the upper left panel of Figure 2.

2.3.2. *Stellar Rotation Periods*

An independent way to assess the age of the candidate cluster members is to measure their stellar rotation periods. This approach can be achieved using surveys such as TESS (Ricker et al. 2015) and the Zwicky Transient Facility (ZTF, Bellm et al. 2019); it leverages a storied tradition of measuring rotation periods of stars in benchmark open clusters (see e.g., Skumanich 1972; Curtis et al. 2020). The TESS data in our case are especially useful, since they provide 3 to 5 lunar months of photometry for all of our candidate CH-2 and RSG-5 members.

We selected stars suitable for gyrochronology by requiring $(G_{\rm BP}-G_{\rm RP})_0 \geq 0.5$ to focus on FGKM stars that experience magnetic braking. For TESS, we also restricted our sample to $G < 16$, to ensure the stars are bright enough to extract usable light curves from the full-frame images. The magnitude cut corresponds to $(G_{\rm BP}-G_{\rm RP})_0 < 2.6$ ($\sim$M3V) at the relevant distances. These cuts gave 19 stars in CH-2 and 47 stars in RSG-5. We extracted light curves from the TESS images using the `unpopular` package (Hattori et al. 2021), and regressed them against systematics with its causal pixel model. We measured rotation periods using Lomb-Scargle periodograms and visually vetted the results using an interactive program that allows us to switch between TESS Cycles, select particular sectors, flag stars with multiple periods, and correct half-period harmonics. For ZTF, we used the same color cut to focus on FGKM stars, but restricted the sample to $13 < G < 18$ to avoid the saturation limit on the bright end and ensure sufficient photometric precision at the faint end. We followed the procedure outlined in Curtis et al. (2020): we downloaded $8' \times 8'$ image cutouts, ran aperture photometry for the target and neighboring stars identified with Gaia, and used them to define a systematics correction to refine the target light curves.

The lower panels of Figure 2 show the results. In RSG-5, 41/47 stars have rotation periods faster than the Pleiades (87%). This numerator omits the two stars with periods >12 days visible in the lower-left panel of Figure 2. The age interpretation for these latter stars, particularly the $\approx$M2.5 dwarf, is not obvious. Rebull et al. (2018) for instance have found numerous M-dwarfs with 10-12 day rotation periods at ages of USco ($\sim$8 Myr), and some may still exist at ages of LCC ($\sim$16 Myr; L. Rebull submitted). Regardless, since nearly no field star outliers seem to be present on the RSG-5 CAMD, the fact that we do not detect rotation periods for $\approx$13% of stars should perhaps be taken as an indication for the fraction of stars for which rotation periods might not be detectable, due to e.g., pole-on stars having lower amplitude starspot modulation.

For CH-2, 13/19 stars have rotation periods that are obviously faster than their counterparts in the Pleiades (68%). 4 stars, not included in the preceding numerator, are M-dwarfs with rotation periods between 10 and 12.5 days. As just discussed, the age interpretation for these M-dwarfs is not obvious. Regardless, the $\approx$15% false positive rate for CH-2 determined from the CAMD seems consistent with our fraction of detected rotation periods; RSG-5 was missing rotation periods for ≈15% of its candidate members, even though all of its stars appear photometrically consistent with being on a single pre-main-sequence locus.

It is challenging to convert these stellar rotation periods to a precise age estimate, since on the pre-main-sequence the stars are spinning up due to thermal contraction rather than down due to magnetized braking. Regardless, the rotation period distributions of both CH-2 and RSG-5 seem consistent with other 30 Myr to 50 Myr clusters (e.g., IC 2602 and IC 2391; Douglas et al. 2021). They also seem consistent with the false positive rates estimated from the color–absolute magnitude diagrams.

3. THE STARS

A few salient properties of the Kepler objects in Cep-Her can be gleaned from Figure 2. The stars span spectral types of G8V (Kepler-1627) to K6V (KOI-7913 A). The secondary in the KOI-7913 system has spectral type ≈K8V. And since a star with Solar mass and metallicity arrives at the zero-age main sequence at $t \approx 40$ Myr (Choi et al. 2016), these stars are all in the late stages of their pre-main-sequence contraction.

The adopted stellar parameters are listed in Table 1. The stellar surface gravity, radius, mass, and density are found by interpolating against the MIST isochrones (Choi et al. 2016). The statistical uncertainties from this technique mostly originate from the parallax uncertainties; the systematic uncertainties are taken to be the absolute difference between the PARSEC (Bressan et al. 2012) and MIST isochrones. Reported uncertainties are a quadrature sum of the statistical and systematic components.

To verify these parameters and to analyze youth proxies such as the Li 6708 Å doublet and Hα, we acquired spectra. We also acquired high resolution imaging for each system, to constrain the existence of visual companions, including possible bound binaries. The system-by-system details follow, and the relevant results are also summarized in Table 1.

3.1. *Kepler 1643*

Spectra—For Kepler-1643, we acquired two iodine-free spectra from Keck/HIRES on the nights of 2020 Aug 16 and 2021 Oct 25. The acquisition and analysis followed the usual techniques of the California Planet Survey (Howard et al. 2010). We derived the stellar parameters ($T_{\rm eff}, \log g, R_\star$) using `SpecMatch-Emp` (Yee et al. 2017), which yielded values in <1-σ agreement with those from the cluster-isochrone method. This approach also yielded [Fe/H] = 0.13 ± 0.09. Using the broadened synthetic templates from `SpecMatch-Synth` (Petigura et al. 2017), we found $v \sin i = 9.3 \pm 1.0\,{\rm km\,s^{-1}}$. The systemic radial velocity

Table 1. Selected system parameters of Kepler-1643, KOI-7368, and KOI-7913.

Parameter	Value	Uncertainty	Comment
	Kepler-1643		
Stellar parameters:			
Gaia G [mag]	13.836	±0.003	A
$T_{\rm eff}$ [K]	4916	±110	B
$\log g_\star$ [cgs]	4.502	±0.035	C
$R_\star$ [$R_\odot$]	0.855	±0.044	C
$M_\star$ [$M_\odot$]	0.845	±0.025	C
$\rho_\star$ [g cm^{-3}]	1.910	±0.271	C
$P_{\rm rot}$ [days]	5.106	±0.044	D
Li EW [mÅ]	130	+6, −5	E
Transit parameters:			
P [days]	5.3426258	±0.0000101	D
$R_{\rm p}/R_\star$	0.025	±0.001	D
b	0.58	±0.05	D
$R_{\rm p}$ [$R_\oplus$]	2.32	±0.14	D
t_{14} [hours]	2.409	±0.061	D
	KOI-7368		
Stellar parameters:			
Gaia G [mag]	12.831	±0.004	A
$T_{\rm eff}$ [K]	5241	±50	F
$\log g_\star$ [cgs]	4.499	±0.030	C
$R_\star$ [$R_\odot$]	0.876	±0.035	C
$M_\star$ [$M_\odot$]	0.879	±0.018	C
$\rho_\star$ [g cm^{-3}]	1.840	±0.225	C
$P_{\rm rot}$ [days]	2.606	±0.038	D
Li EW [mÅ]	236	+16, −14	E
Transit parameters:			
P [days]	6.8430341	±0.0000125	D
$R_{\rm p}/R_\star$	0.023	±0.01	D
b	0.50	±0.06	D
$R_{\rm p}$ [$R_\oplus$]	2.22	±0.12	D
t_{14} [hours]	2.792	±0.075	D
	KOI-7913		
Stellar parameters:			
Gaia G [mag]	14.200	±0.003	A
$T_{\rm eff,A}$ [K]	4324	±70	B
$T_{\rm eff,B}$ [K]	4038	±70	B
$\log g_{\star,A}$ [cgs]	4.523	±0.043	C
$R_{\star,A}$ [$R_\odot$]	0.790	±0.049	C
$M_{\star,A}$ [$M_\odot$]	0.760	±0.025	C
$\rho_{\star,A}$ [g cm^{-3}]	2.172	±0.379	C
$P_{\rm rot,A}$ [days]	3.387	±0.016	D
$P_{\rm rot,B}$ [days]	2.642	±0.067	D
(Li EW)$_{\rm A}$ [mÅ]	65	+8, −6	E
(Li EW)$_{\rm B}$ [mÅ]	42	+12, −19	E
$\Delta G_{\rm AB}$ [mag]	0.51	±0.01	G
Apparent sep. [au]	959.4	±1.9	G
Transit parameters:			
P [days]	24.2785706	±0.0002630	D
$R_{\rm p}/R_\star$	0.027	±0.001	D
b	0.30	±0.15	D
$R_{\rm p}$ [$R_\oplus$]	2.34	±0.18	D
t_{14} [hours]	4.396	0.207	D

NOTE— (A) Gaia Collaboration et al. (2021a). (B) HIRES SpecMatch-Emp (Yee et al. 2017). (C) Cluster isochrone (Choi et al. 2016; Bressan et al. 2012). (D) Kepler light curve. The full set of transit parameters are given in Appendix C. (E) HIRES/TRES (Bouma et al. 2021). (F) TRES SPC (?Bieryla et al. 2021). (G) Magnitude difference and apparent physical separation between primary and secondary; from Gaia EDR3. (H) HIRES SpecMatch-Synth (Petigura et al. 2017).

at the two epochs was -9.1 ± 1.9 km s^{-1} and -7.8 ± 1.2 km s^{-1} respectively (Chubak et al. 2012). To infer the equivalent width of the Li I 6708 Å doublet, we followed the procedure described by Bouma et al. (2021). This yielded a strong detection: $\mathrm{EW_{Li}} = 130^{+6}_{-5}$ mÅ, with values consistent at $<$1-σ between the two epochs. The quoted value does not correct for the Fe I blend at 6707.44 Å. Given the purported age and effective temperature of the star, the lithium equivalent width is somewhat low. We discuss this in greater depth in Appendix B.

High-Resolution Imaging —We acquired adaptive optics imaging of Kepler-1643 on the night of 2019 June 28 using the NIRC2 imager on Keck-II. Using the narrow camera (FOV = 10.2″), we obtained 4 images in the K' filter ($\lambda = 2.12\,\mu$m) with a total exposure time of 320 s. The images did not show any additional visual companions. We analyzed the data following Kraus et al. (2016), and determined the detection limits by analyzing the residuals after subtracting an empirical PSF template. This procedure yielded contrast limits of $\Delta K' = 4.1$ mag at $\rho = 150$ mas, $\Delta K' = 5.8$ mag at $\rho = 300$ mas, and $\Delta K' = 8.3$ mag at $\rho > 1000$ mas.

3.2. *KOI-7368*

Spectra —For KOI-7368, we acquired a spectrum on 2015 June 1 using the echelle spectrograph (TRES; Fűrész et al. 2008) mounted at the Tillinghast 1.5m at the Fred Lawrence Whipple Observatory. The Stellar Parameter Classification pipeline for TRES has been described by Bieryla et al. (2021). It is based on the synthetic template library constructed by Buchhave et al. (2012). The resulting stellar parameters ($T_{\rm eff}, \log g, R_\star$) agreed with those from the cluster-isochrone method within 1-σ, though the effective temperature was more precise by a factor of three. Auxiliary spectroscopic parameters included the metallicity [Fe/H] $= -0.02 \pm 0.08$, the equatorial velocity $v \sin i = 20.21 \pm 0.50$ km s^{-1}, and the systemic velocity $\mathrm{RV_{sys}} = -10.9 \pm 0.2$ km s^{-1}. The Li 6708Å EW measurement procedure yielded $\mathrm{EW_{Li}} = 236^{+16}_{-14}$ mÅ.

High-Resolution Imaging —We acquired adaptive optics imaging of KOI-7368 on the night of 2019 June 12, again using NIRC2. The observational configuration and reduction were identical as for Kepler-1643. No companions were detected, and the analysis of the image residuals yielded contrast limits of $\Delta K' = 5.2$ mag at $\rho = 150$ mas, $\Delta K' = 6.7$ mag at $\rho = 300$ mas, and $\Delta K' = 8.7$ mag at $\rho > 1000$ mas.

3.3. *KOI-7913*

Binarity —KOI-7913 is a binary. The north-west primary is ≈0.5 magnitudes brighter than the south-east secondary in optical passbands. The two stars are separated in Gaia EDR3 by 3.″5 on-sky, and have parallaxes consistent within 1-σ (with an average $\varpi = 3.66 \pm 0.01$ mas). The apparent on-sky separation is 959 ± 2 au. The Gaia EDR3 proper motions are also very similar. Since two stars were resolved in the Kepler Input Catalog and are roughly one Kepler pixel apart, an accurate crowding metric has already been applied in the NASA Ames data products to correct the mean flux level (Morris et al. 2017). This is important for deriving accurate transit depths.

Spectra —We acquired Keck/HIRES spectra for KOI-7913 A on the night of 2021 Nov 13, and KOI-7913 B on the night of 2021 Oct 26. The `SpecMatch-Emp` machinery yielded $T_{\rm eff,A} = 4324 \pm 70$ K, and $T_{\rm eff,B} = 4038 \pm 70$ K. The remaining parameters were in agreement with those from the cluster isochrone. For the primary, we also found [Fe/H] $= -0.06 \pm 0.09$, $v \sin i = 13.3 \pm 1.0$ km s^{-1}, and $\mathrm{RV_{sys}} = -17.8 \pm 1.1$ km s^{-1}. For the secondary, these same parameters were [Fe/H] $= -0.01 \pm 0.09$, $v \sin i = 10.7 \pm 1.0$ km s^{-1}, and $\mathrm{RV_{sys}} = -18.8 \pm 1.1$ km s^{-1}. Neither of the KOI-7913 components shows strong lithium absorption, but this is expected given their ≈K6V and ≈K8V spectral types. They do however both show Hα in emission. Broadly speaking, both observations are consistent with a ≈40 Myr age for KOI-7913 (see Appendix B).

High-Resolution Imaging —We acquired adaptive optics imaging of KOI-7913 on the night of 2020 Aug 27 using the NIRC2 imager. The observational configuration and reduction were identical as before. The images showed KOI-7913 A, KOI-7913 B, and an additional faint star ≈0.″99 due East of KOI-7913 B. Applying the PSF-fitting routines from Kraus et al. (2016), the tertiary star has a separation $\rho = 4397 \pm 3$ mas from the primary, at a position angle $231.17^\circ \pm 0.02^\circ$, with $\Delta K' = 6.97 \pm 0.04$. While it is too faint to affect the interpretation of the KOI itself, it would be amusing if the faint neighbor were also comoving and young – at the age of the system, it would have a mass between 10 and 15 $\mathrm{M_{Jup}}$. Additional imaging epochs will tell.

4. THE PLANETS

4.1. *Kepler Data*

The Kepler space telescope observed Kepler-1643, KOI-7913, and KOI-7368 at a 30-minute cadence between May 2009 and April 2013. For all three systems quarters 1 through 17 were observed with minimal data gaps. The top panel of Figure 3 shows a 50-day slice of the `PDCSAP` light curves for the three new Cep-Her candidates, along with Kepler-1627. In `PDCSAP`, non-astrophysical variability is removed through a cotrending approach that uses a set of basis vectors derived by applying singular value decomposition to a set of systematics-dominated light curves (Smith et al. 2017). In our analysis, we used the `PDCSAP` light curves with the default optimal aperture (Smith et al. 2016). Cadences with

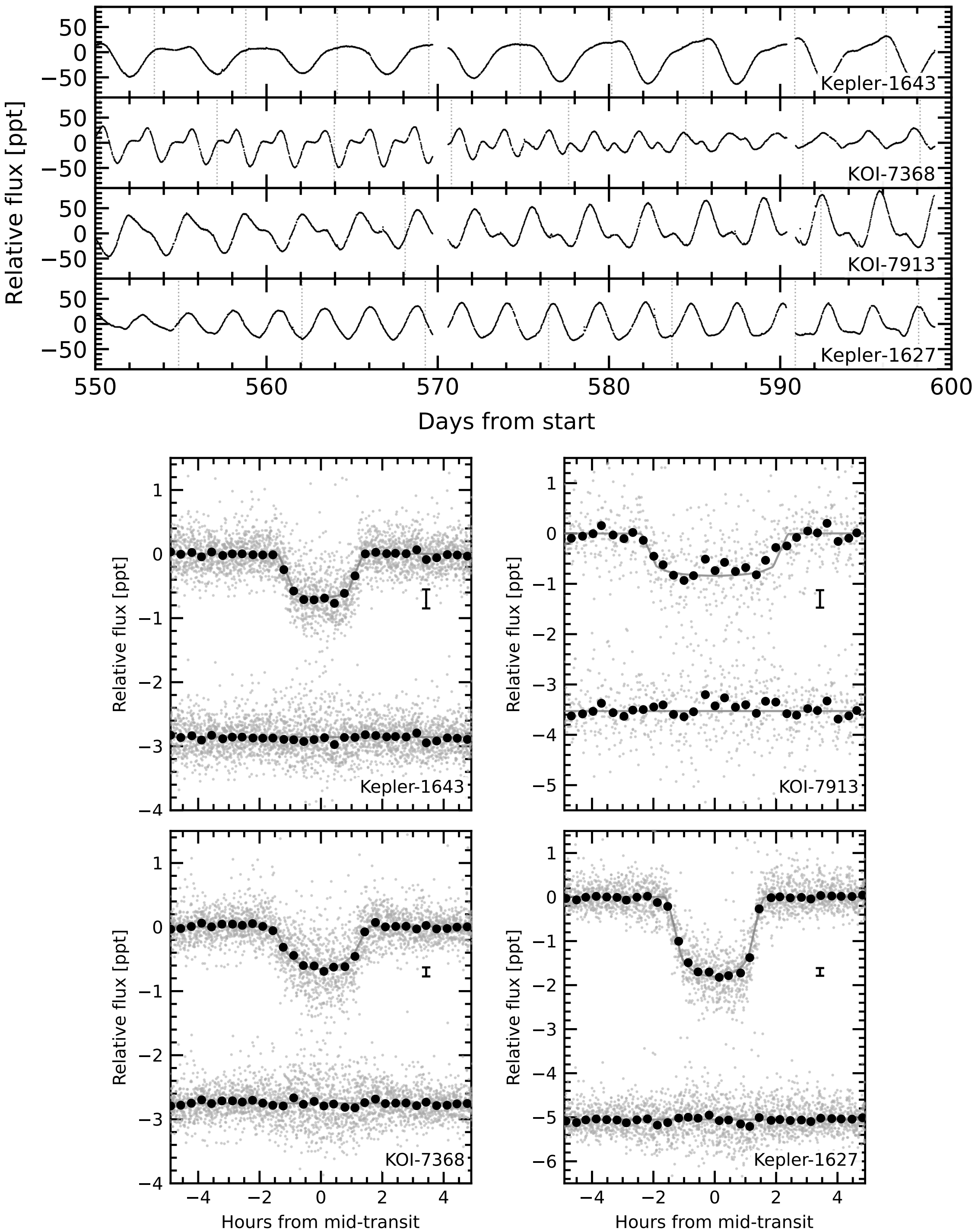

Figure 3. Raw and processed light curves for the Kepler Objects of Interest in Cep-Her. *Top*: 50 day light curve segment from the 3.9 years of Kepler data. The ordinate shows the `PDCSAP` median-subtracted flux in units of parts-per-thousand ($\times10^{-3}$). The dominant signal is from starspots; planetary transit times are indicated but the individual transits are not visible at this scale. *Bottom*: Phase-folded transits of Kepler-1643, KOI-7913, KOI-7368, and Kepler-1627 with stellar variability removed. The maximum a posteriori model is shown with the gray line, and the residual after subtracting the transit model is vertically displaced. Windows over 10 hours are shown. Gray points are individual flux measurements; black points are binned to 20 minute intervals, and have a representative 1-σ error bar in the center-right of each panel.

non-zero quality flags were omitted. In all cases, the stars are dominated by spot-induced modulation with peak-to-peak variability between 2% and 10%. These signals are much larger than the transits, which have depth ≈0.1%. To quantify the stellar rotation periods, we calculated the Lomb-Scargle periodogram for each Kepler quarter independently. The resulting means and standard deviations are in Table 1.

4.2. *Transit and Stellar Variability Model*

Our goals in fitting the Kepler light curves are twofold. First, we want to derive accurate planetary sizes and orbital properties. Second, we want to remove the spot-induced variability signal to enable a statistical assessment of the probability that the transit signals are planetary.

We fitted the data as follows. Given the transit ephemeris from Thompson et al. (2018), we first trimmed the light curve to a local window around each transit that spanned three transit durations before and after each transit midpoint. The out-of-transit points in each local window were then fitted with a fourth-order polynomial, which was divided out from the light curve. The resulting flattened transits were then fitted with a transit model that assumed quadratic limb darkening. The model therefore included 8 free parameters for the transit ($\{P, t_0, \log R_{\rm p}/R_\star, b, u_1, u_2, R_\star, \log g\}$), 2 free parameters for the light curve normalization and a white noise jitter ($\{\langle f \rangle, \sigma_f\}$), and 5 fixed parameters for each transit.

We fitted the data using `exoplanet` (Foreman-Mackey et al. 2020). We assumed a Gaussian likelihood, and sampled using `PyMC3`'s No-U-Turn Sampler (Hoffman & Gelman 2014), after having initialized to the the maximum a posteriori (MAP) model. We used the Gelman & Rubin (1992) statistic, $\hat{R}$, as our convergence diagnostic. The resulting fits are shown in the lower panels of Figure 3, and the important derived parameters are in Table 1. The set of full parameters and their priors are given in Appendix C.

A potential drawback of our approach is that to remove the starspot-induced variability, we fixed 5 parameters per transit to their MAP values. An alternative could be to fit the planetary transits simultaneously with the starspot-induced variability using a quasiperiodic Gaussian process (GP). We explored this approach, but found that it often required fine-tuning of the hyperparameter priors, otherwise the GP would overfit flares, instrumental noise, and any other variability that was not part of the transit. This failure mode is pernicious, in that it yields an ill-founded sense of confidence in a visually clean fit. Our model is simpler, and it has the benefit that the white noise jitter never trades off with any parameter equivalent to a damping timescale for the coherence of the GP. It is also computationally efficient, and it captures the planetary parameters about which we care the most.

4.3. *Planet Validation*

In the future, it may be possible to obtain independent evidence for the planetary nature of the Cep-Her planets, for instance by observing spectroscopic transits. For now, it is of interest whether the transit signals might be astrophysical false positives, or whether they are statistically more likely to be planetary. We adopt the Bayesian framework implemented in `VESPA` to assess the relevant probabilities (Morton 2012, 2015). Briefly summarized, the priors in `VESPA` assume the binary star occurrence rate from Raghavan et al. (2010), direction-specific star counts from Girardi et al. (2005), and planet occurrence rates as described by Morton (2012, Section 3.4). The likelihoods are then evaluated by forward-modeling a synthetic population of eclipsing bodies for each astrophysical model class, in which each population member has a known trapezoidal eclipse depth, total duration, and ingress duration. These summary statistics are then compared against the actual photometric data to evaluate the probabilities of false positive scenarios such as foreground eclipsing binaries, hierarchical eclipsing binaries, and background eclipsing binaries.

Kepler-1643 —Kepler-1643 b (KOI-6186.01) was already validated as a transiting planet by Morton et al. (2016), who found a probability for any of the aforementioned false positive scenarios of 9×10^{-6}. Repeating the calculation with our own stellar-variability correction and the new NIRC2 imaging constraints, we find FPP = 6×10^{-9}. Figure 3 shows the justification: the transit is flat and has a high S/N (≈47). The shape is therefore nearly impossible to reproduce with eclipsing binary models.

Intriguingly, Kepler-1643 failed one of the data validation centroid shift tests (see the `q1_q17_dr25_koi` data release): the angular distance between the target star's catalog position and the position of the transiting source was measured as $1\farcs0$ at 4.4-σ. The reports show however that two outlying quarters (2 and 6) drive the offset — the centroid locations from the other Kepler quarters are consistent at $\lesssim 0\farcs4$. This is an instructive exercise in how stellar variability complicates centroid-based vetting tests. The shifts measured by these tests are determined from the in- and out-of-transit flux-weighted centroids. For stars with significant spot-induced variability there is no static baseline in either the in- or out-of-transit phases.

KOI-7368 —KOI-7368.01 is listed on the NASA Exoplanet Archive as a "candidate" planet. Morton et al. (2016) did not compute a false positive probability for the system because their default trapezoidal fitting routine failed, presumably due to the spot-induced variability. Our fitting approach rectifies this point, and our new NIRC2 images revealed no new stellar companions. Performing the relevant calculation, we find FPP = 4×10^{-3}. Though not as convincing as Kepler-1643, this clears the usual threshold for calling the planet statistically validated (Morton 2012). The S/N of the transit is ≈32, which indicates that it is unlikely to be caused by systematic noise in the light curve (see Figure 3). The positional probability score also meets the requirements for transiting sources thought to share positions with their target stars (Bryson & Morton 2017).

It bears mentioning that KOI-7368 shows a centroid shift in the `q1_q17_dr25_koi` validation reports, similar to Kepler-1643. For KOI-7368, the reported offset is smaller, and less significant ($0\farcs2$; 3.0-σ). Again, the data validation reports show that the shift is caused by a few outlying quarters (4, 5, 8, and 12). Since the remaining data show consistent scatter in their centroid locations, these outlying quarters are likely also caused by the stellar variability. Our NIRC2 imaging independently shows that there are no neighboring sources that could cause an offset of the observed amplitude.

KOI-7913—KOI-7913.01 is also currently listed on the NASA Exoplanet Archive as a "candidate" planet. The Morton et al. (2016) analysis was of Q1-Q17 KOIs from DR24, and therefore spanned KOI-1.01 to KOI-7620.01 (omitting KOI-7913.01). However the results of the subsequent DR25 analysis by Morton et al. are listed at the NASA Exoplanet Archive. The relevant table gives a probability for the system being an astrophysical false positive of 1.4×10^{-4}, with the most likely false positive scenario being a blended eclipsing binary. Repeating the calculation with our new detrending and NIRC2 contrast curves, we find a similar result: FPP = 1.3×10^{-4}. Though the transit has the lowest S/N of any of the objects discussed (≈14), its lower FPP relative to KOI-7368 can be understood through its flat-bottomed shape, combined with its long transit duration relative to most eclipsing binary models (Figure 3). The host star probability usability score (Bryson & Morton 2017) also meets the usual threshold, and so the planet is statistically validated. Its disposition has however previously fluctuated from "false positive" to "candidate" (see Appendix D). The most likely explanation is the presence of KOI-7913 B, which is located ≈ 0.9 Kepler pixels away from Kepler-7913 A. While the ≈1.5 pixel FWHM of the Kepler pixel response function implies that there is blending between the two stars, the target-pixel level data for KOI-7913 B reveals an entirely different stellar rotation period (Table 1), and no hint of the transit signal. This implies that KOI-7913 B cannot host the planet.

5. DISCUSSION & CONCLUSION

5.1. *Normal-Sized Mini-Neptunes Exist at 40 Myr*

The most significant novelty about the planets in Kepler-1643, KOI-7368, and KOI-7913 is that their sizes are normal relative to the known population of mini-Neptunes from Kepler. At field star ages, mini-Neptune sizes span $1.8\,R_\oplus$ to $3.6\,R_\oplus$, with the most common size being $\approx 2.4\,R_\oplus$ (Fulton et al. 2017, Figure 7). The known planets younger than 10^8 years are almost all larger, with sizes between 4 and $10\,R_\oplus$ (Mann et al. 2016; David et al. 2016; Benatti et al. 2019; David et al. 2019; Newton et al. 2019; Rizzuto et al. 2020; Bouma et al. 2020; Mann et al. 2022). Figure 4 explores this in more detail by showing the sizes, orbital periods, and ages of the known transiting planets, emphasizing planets with precise ages. The smallest previously known planets comparable to the new Cep-Her mini-Neptunes are AU Mic c ($3.0 \pm 0.2\,R_\oplus$, see Martioli et al. 2021 and Gilbert et al. 2022), Kepler-1627 Ab ($3.8 \pm 0.2\,R_\oplus$; Bouma et al. 2022), and AU Mic d ($4.2 \pm 0.2\,R_\oplus$; Plavchan et al. 2020).

The theoretical expectation is that mini-Neptunes with sizes of 2 to $3\,R_\oplus$ should be common at ages of 10^7 to 10^8 years. This expectation is tied to inferences about the initial distributions of planetary core mass, core composition, and atmospheric mass fraction (Owen & Wu 2017). The Kelvin-Helmholtz cooling timescale, which is tied to the entropy of the planetary interior shortly after disk dispersal, also plays a significant role (Owen 2020). As an example, Rogers & Owen (2021) predicted that given a core-mass distribution peaked at $\approx 4\,M_\oplus$, an ice-poor rock/iron core composition, and a typical H/He mass fraction of ≈4%, there should be a maximum in planet occurrence at 2 to $3\,R_\oplus$ at times between 10 and 100 Myr. The models advanced by Gupta & Schlichting (2020) and Lee & Connors (2021) agree; their differences lie in the mechanism for producing the radius valley.

Systems such as K2-25, V1298 Tau, HIP-67522, TOI-837, and TOI-1227 have sizes that are anomalously large relative to the predicted peak in planet occurrence at 2 to $3\,R_\oplus$. However, their large sizes can be accommodated by invoking any of *i)* larger core masses, *ii)* more volatile-rich compositions, *iii)* larger initial atmospheric mass fractions, or *iv)* longer thermal cooling times. Secure mass measurements would help constrain this parameter space, but the ~ 1 km s^{-1} spot-induced radial velocity semi-amplitudes makes measuring the Doppler orbits very difficult. (Cale et al. 2021; Zicher et al. 2022; Klein et al. 2022). Regardless, the new Kepler-1643, KOI-7368, and KOI-7913 systems do demonstrate that at least some planets at 40 Myr have sizes that are consistent with theoretical expectations for mini-Neptunes. While selection effects imposed by spot-induced photometric variability are a likely explanation for why planets this small have not previously been identified (e.g., Zhou et al. 2021), future work should quantify this bias more carefully, in order to enable empirical studies of how the planetary size distribution changes at early times.

5.2. *Is CH-2 real?*

RSG-5, and Kepler-1643's membership inside it, meet typical expectations for a star claimed to be in an open cluster. RSG-5 is an obvious overdensity relative to the local field, and our membership selection easily produces a clean

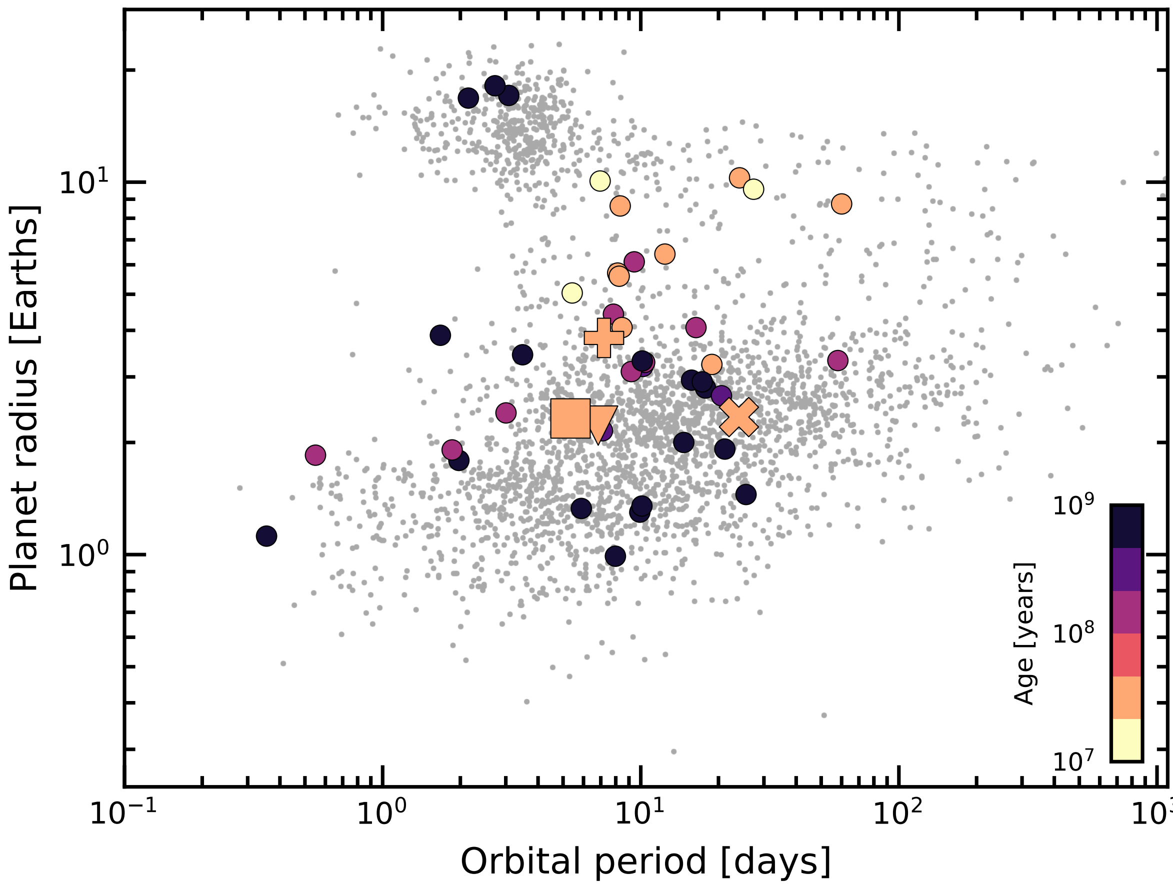

Figure 4. Radii, orbital periods, and ages of transiting exoplanets. Planets younger than a gigayear with ages more precise than a factor of three are emphasized. The Cep-Her planets are Kepler-1643 b (□), KOI-7368 b (▽), KOI-7913 Ab (X), and Kepler-1627 Ab (+). Interesting trends in the population of planets younger than 10^8 years old include *i)* their large sizes and *ii)* the lack of hot Jupiters. The new objects of interest in Cep-Her have normal mini-Neptune sizes between 2 and $3\,R_\oplus$, which is a novelty given their ages. Parameters are from the NASA Exoplanet Archive (2022 Apr 5).

pre-main-sequence locus in color versus absolute magnitude (Figure 2). CH-2, and KOI-7913 and KOI-7368's membership inside it, do not meet these expectations in as obvious a manner. This is because the CH-2 association is diffuse.

To quantify the density difference between CH-2 and RSG-5, we can compare the spatial and velocity volumes searched for each group. For RSG-5, we drew 173 candidate members from a $30\,\mathrm{pc} \times 30\,\mathrm{pc} \times 40\,\mathrm{pc}$ rectangular prism, given a $1.5\,\mathrm{km\,s^{-1}} \times 2.5\,\mathrm{km\,s^{-1}}$ rectangle in apparent galactic velocity. For CH-2, our 37 candidate members came from a rectangular prism of dimension $50\,\mathrm{pc} \times 40\,\mathrm{pc} \times 30\,\mathrm{pc}$, and a rectangular box of $2\,\mathrm{km\,s^{-1}} \times 4\,\mathrm{km\,s^{-1}}$. If we define the searched volume in units of $\mathrm{pc^3\,km^2\,s^{-2}}$, then the volume ratio of CH-2 to RSG-5 is 3.5 to 1. The ratio of number densities (candidate members per unit searched volume) in RSG-5 relative to CH-2 is 16 to 1.

Given its low density, in CH-2 really a star cluster? For this discussion, we adopt the definition that a star cluster is a group of at least 12 stars that was physically associated at its time of formation. The "12" is set to distinguish star clusters from high-order multiples (see Krumholz et al. 2019). We explicitly do not require a "star cluster" to be gravitationally bound: dissolved clusters as well as their tidal tails are included in our adopted definition of "clusters". We similarly do not require a threshold number of stars per unit spatial volume. The latter point acknowledges that an important factor in cluster identification is also density in velocity space. Perhaps once stellar rotation periods and chemical abundances reach the same level of ubiquity as stellar proper motions, they might enable further refinement of our ability to discover stars that formed as part of the same event.

From a data-driven perspective, demonstrating that a group of stars was physically associated at its time of formation is challenging. While some young groups show kinematic evidence for expansion (Kuhn et al. 2019), many, including Sco-Cen, do not (Wright & Mamajek 2018). This complicates the feasibility of deriving kinematic ages through traceback, as well as through the expansion itself (see Crundall et al. 2019). A more minimal approach is that suggested by Tofflemire et al. (2021): search for coeval, phase-space neighbors, measure their ages, and determine if they share a common age. This approach can demonstrate whether a star is currently associated with a set of coeval stars, though it falls short of determining what the association looked like in the past. Our analysis of CH-2 meets the latter standard for the existence of a $\approx$40 Myr stellar association. It would be a worthy exercise for future work to perform a similar search for coeval phase-space neighbors on the entire dataset of known exoplanet hosts. For the time being, we can offer the anecdotal point that in our experience, most stars do not have dozens of 40 Myr neighbors within a local volume of a few $\mathrm{km\,s^{-1}}$ and tens of parsecs.

5.3. *Future work*

Cep-Her—Our analysis to date has focused only on portions of Cep-Her that were observed by Kepler: RSG-5, CH-2, and the δ Lyr cluster. In Bouma et al. (2022) as well as this work, we have shown that these groups share similar ages, and have kinematic correlations that suggest a common origin. With that said, the membership and kinematics of the other Cep-Her groups shown in Figure 1 deserve independent attention. An important aspect of the remaining work will be to acquire radial velocities of a large subset of the stars, to assess whether the traceback approach could be applicable. Wide-field spectroscopic surveys such as LAMOST (Zhao et al. 2012) or SDSS-V (Kollmeier et al. 2017) could enable such analyses, while also providing sensitivity to the Li 6708 Å line. If Gaia DR3 provides RVS spectra for the brighter F and G dwarfs, these would also contain the calcium infrared triplet as another age indicator. These indicators, combined with better kinematics, would help in definitively unraveling the formation history of the complex.

A number of worthy photometric projects also seem possible given the new understanding of Cep-Her. One is asteroseismology of the δ Sct stars, using either TESS or Kepler data (Bedding et al. 2020). For cases in which the modes are resolved, this might yield age or metallicity estimates for the subgroups independent of other methods. Other projects could include a more comprehensive analysis of the stellar rotation periods, searches of the Kepler light curves for exocomets (Zieba et al. 2019), and searches for missed planets around the most rapid rotators.

Exoplanet demographics at early times—Our main motivation for finding new young planets is to help benchmark models for planetary evolution. However demographic analyses of the known planets between 10^7 and 10^9 years have so far been rather limited. Approximately 40 such planets are now known (Figure 2). About half come from K2, a quarter from TESS, and now a quarter from Kepler.

Given the current state of the field, a few reflections regarding experimental design of a demographic survey focused on planetary evolution over the first gigayear might be useful. The first is that such a project requires a set of target stars with known ages. A promising way to compile relevant stars could be to combine automated spatio-kinematic clustering from Gaia with rotation periods measured using TESS (see the appendices of Bouma et al. 2022). The second consideration is that all the known young planets smaller than $3\,R_\oplus$ come from either K2 or Kepler. Demographic inferences based on TESS are therefore limited to planetary sizes $\gtrsim 4\,R_\oplus$, for planets close-in to their host stars. It would be worthwhile to compare the occurrence rates of both types of planets with those from the main Kepler sample. One specific question that seems within reach would be to clarify whether enough young stars have been searched for the dearth of young hot Jupiters to be significant. Since the hot Jupiter occurrence rate is strongly dependent on stellar mass and metallicity (Petigura et al. 2018, 2022), particular care would be needed to select a sample of well-studied FGK dwarfs for the measurement, likely using stars in Sco OB2, Cep-Her, and Orion. For demographic studies focused on how mini-Neptune sizes evolve, the combined K2 and Kepler dataset would be the better primary source.

5.4. *Summary*

We have shown that Kepler-1643 b, KOI-7368 b, and KOI-7913 Ab are 40 to 50 million years old, and that each system is most likely planetary. The evidence for the planetary interpretation comes from an application of `VESPA` to the Kepler data, alongside new imaging from NIRC2. The validity of the `VESPA` framework rests on the premise that non-astrophysical false positives can be rejected. Kepler-1643 and KOI-7368 both pass all but one of the canonical vetting tests: the check for centroid offsets between the in and out-of-transit phases. For both cases, the weak observed shifts are consistent with being caused by starspot-induced variability in specific quarters spuriously moving the stellar center-of-light. Independently, our imaging rules out companion stars with the brightness and positions that would be needed to otherwise explain the reported shifts.

Each system has multiple indicators of youth that support the reported ages. For Kepler-1643, the strongest youth indicator is its physical and kinematic association with RSG-5. Based on the color–absolute magnitude diagram, we are able to select members of this cluster with a false positive rate of a few percent (Figure 2). Kepler-1643 is one such member. While the stellar rotation period period agrees with this assessment, the star's lithium equivalent width is marginally low, which might motivate future exploration of lithium depletion across FGKM stars in RSG-5 (see Appendix B).

The spatio-kinematic argument for the youth of KOI-7368 and KOI-7913 is weaker because they are in an association of stars, CH-2, that is more diffuse. For KOI-7913, stronger indicators of its age come from its binary. Both stellar components in KOI-7913 have isochronal ages consistent with 40 Myr. Both components also show Hα in emission, which for the $\approx$K6V primary is a strong indicator that the star is $\lesssim$100 Myr old. KOI-7368 is slightly more massive, and the Li 6708 Å measurement and stellar rotation period provide independent verification of the star's youth.

The astrophysical implication of these considerations is that planets $\approx$2 Earth radii in size exist at ages of 40 million years. It will be interesting to continue the push down to smaller planetary sizes at comparable ages – the planetary detections we have presented are well above the average detection significance for Kepler planets. There may still be room at the bottom.

ACKNOWLEDGMENTS

L.G.B. is supported by the Heising-Simons Foundation 51 Pegasi b Fellowship and the TESS GI Program (NASA grants 80NSSC21K0335 and 80NSSC22K0298). R.K. is supported by the Heising-Simons Foundation. J.L.C. is supported by NSF AST-2009840 and the TESS GI Program (NASA grant 80NSSC22K0299).

Software: `astropy` (Astropy Collaboration et al. 2018), `astroquery` (Ginsburg et al. 2018), `exoplanet` (Foreman-Mackey et al. 2020), and its dependencies (Agol et al. 2020; Kipping 2013; Luger et al. 2019; Theano Development Team 2016), `PyMC3` (Salvatier et al. 2016), `tesscut` (Brasseur et al. 2019), `unpopular` (Hattori et al. 2021), `VESPA` (Morton 2012, 2015),

Facilities: *Astrometry*: Gaia (Gaia Collaboration et al. 2018b, 2021a). *Imaging*: Second Generation Digitized Sky Survey. Keck:II (NIRC2; www2.keck.hawaii.edu/inst/nirc2). *Spectroscopy*: Tillinghast:1.5m (TRES; Fűrész et al. 2008). Keck:I (HIRES; Vogt et al. 1994). *Photometry*: Kepler (Borucki et al. 2010), TESS (Ricker et al. 2015), ZTF (Bellm et al. 2019).

REFERENCES

Agol, E., Luger, R., & Foreman-Mackey, D. 2020, AJ, 159, 123

Arevalo, R. T., Tamayo, D., & Cranmer, M. 2022, arXiv:2203.02805 [astro-ph]

Astropy Collaboration, Price-Whelan, A. M., Sipőcz, B. M., et al. 2018, AJ, 156, 123

Bedding, T. R., Murphy, S. J., Hey, D. R., et al. 2020, Nature, 581, 147

Bellm, E. C., Kulkarni, S. R., Graham, M. J., et al. 2019, PASP, 131, 018002

Benatti, S., Nardiello, D., Malavolta, L., et al. 2019, A&A, 630, A81

Berger, T. A., Howard, A. W., & Boesgaard, A. M. 2018, ApJ, 855, 115

Bieryla, A., Tronsgaard, R., Buchhave, L. A., et al. 2021, in Posters from the TESS Science Conference II (TSC2), 124

Binks, A. S., Jeffries, R. D., Sacco, G. G., et al. 2022, arXiv e-prints, arXiv:2204.05820

Borucki, W. J., Koch, D., Basri, G., et al. 2010, Science, 327, 977

Bouma, L. G., Curtis, J. L., Hartman, J. D., Winn, J. N., & Bakos, G. Á. 2021, AJ, 162, 197

Bouma, L. G., Hartman, J. D., Brahm, R., et al. 2020, AJ, 160, 239

Bouma, L. G., Curtis, J. L., Masuda, K., et al. 2022, AJ, 163, 121

Bouvier, J. 2020, Mem. Soc. Astron. Italiana, 91, 39

Bouvier, J., Barrado, D., Moraux, E., et al. 2018, A&A, 613, A63

Brasseur, C. E., Phillip, C., Fleming, S. W., Mullally, S. E., & White, R. L. 2019, Astrophysics Source Code Library, ascl:1905.007

Bressan, A., Marigo, P., Girardi, L., et al. 2012, MNRAS, 427, 127

Bryson, S. T., & Morton, Timothy, D. 2017, Kepler Science Document KSCI-19108-001

Buchhave, L. A., Latham, D., Johansen, A., et al. 2012, Nature, 486, 375

Butler, R. P., Cohen, R. D., Duncan, D. K., & Marcy, G. W. 1987, ApJL, 319, L19

Cale, B. L., Reefe, M., Plavchan, P., et al. 2021, AJ, 162, 295

Campello, R. J. G. B., Moulavi, D., Zimek, A., & Sander, J. 2015, ACM Transactions on Knowledge Discovery from Data, 10, 5:1

Cantat-Gaudin, T., Jordi, C., Vallenari, A., et al. 2018, A&A, 618, A93

Choi, J., Dotter, A., Conroy, C., et al. 2016, ApJ, 823, 102

Chubak, C., Marcy, G., Fischer, D. A., et al. 2012, arXiv e-prints, arXiv:1207.6212

Collins, J. M., Jones, H. R. A., & Barnes, J. R. 2017, a, 602, A48

Crundall, T. D., Ireland, M. J., Krumholz, M. R., et al. 2019, MNRAS, 489, 3625

Curtis, J. L., Agüeros, M. A., Mamajek, E. E., Wright, J. T., & Cummings, J. D. 2019, AJ, 158, 77

Curtis, J. L., Agüeros, M. A., Matt, S. P., et al. 2020, ApJ, 904, 140

Dahm, S. E. 2015, ApJ, 813, 108

Damiani, F., Prisinzano, L., Pillitteri, I., Micela, G., & Sciortino, S. 2019, A&A, 623, A112

David, T. J., & Hillenbrand, L. A. 2015, ApJ, 804, 146

David, T. J., Petigura, E. A., Luger, R., et al. 2019, ApJL, 885, L12

David, T. J., Hillenbrand, L. A., Petigura, E. A., et al. 2016, Nature, 534, 658

Dawson, R. I., & Johnson, J. A. 2018, ARA&A, 56, 175

Dinnbier, F., & Kroupa, P. 2020, a, 640, A85

Douglas, S. T., Agüeros, M. A., Covey, K. R., & Kraus, A. 2017, ApJ, 842, 83

Douglas, S. T., Pérez Chávez, J., Cargile, P. A., et al. 2021, 10.5281/zenodo.5131306

Fűrész, G., Szentgyorgyi, A. H., & Meibom, S. 2008, in Precision Spectroscopy in Astrophysics, ed. N. C. Santos, L. Pasquini, A. C. M. Correia, & M. Romaniello, 287

Foreman-Mackey, D., Czekala, I., Luger, R., et al. 2020, exoplanet-dev/exoplanet v0.2.6

Fuhrmeister, B., Schmitt, J. H. M. M., & Hauschildt, P. H. 2005, A&A, 439, 1137

Fulton, B. J., Petigura, E. A., Howard, A. W., et al. 2017, AJ, 154, 109

Gagné, J., Faherty, J. K., Moranta, L., & Popinchalk, M. 2021, ApJL, 915, L29

Gagné, J., David, T. J., Mamajek, E. E., et al. 2020, ApJ, 903, 96

Gaia Collaboration, Babusiaux, C., van Leeuwen, F., et al. 2018a, A&A, 616, A10

Gaia Collaboration, Brown, A. G. A., Vallenari, A., et al. 2018b, A&A, 616, A1

—. 2021a, A&A, 649, A1

Gaia Collaboration, Smart, R. L., Sarro, L. M., et al. 2021b, A&A, 649, A6

Gelman, A., & Rubin, D. B. 1992, Statistical Science, 7, 457, publisher: Institute of Mathematical Statistics

Gilbert, E. A., Barclay, T., Quintana, E. V., et al. 2022, AJ, 163, 147

Ginsburg, A., Sipocz, B., Madhura Parikh, et al. 2018, Astropy/Astroquery: V0.3.7 Release

Ginzburg, S., Schlichting, H. E., & Sari, R. 2018, MNRAS, 476, 759

Girardi, L., Groenewegen, M. A. T., Hatziminaoglou, E., & da Costa, L. 2005, A&A, 436, 895

Goldberg, M., & Batygin, K. 2022, arXiv:2203.00801 [astro-ph]

Gupta, A., & Schlichting, H. E. 2020, MNRAS, 493, 792

Hattori, S., Foreman-Mackey, D., Hogg, D. W., et al. 2021, arXiv e-prints, arXiv:2106.15063

Hawkins, K., Lucey, M., & Curtis, J. 2020, MNRAS, 496, 2422

Hedges, C., Hughes, A., Zhou, G., et al. 2021, AJ, 162, 54

Hoffman, M. D., & Gelman, A. 2014, Journal of Machine Learning Research, 15, 1593

Howard, A. W., Johnson, J. A., Marcy, G. W., et al. 2010, ApJ, 721, 1467
Izidoro, A., Ogihara, M., Raymond, S. N., et al. 2017, MNRAS, 470, 1750
Jerabkova, T., Boffin, H. M. J., Beccari, G., et al. 2021, A&A, 647, A137
Jones, B. F., Shetrone, M., Fischer, D., & Soderblom, D. R. 1996, AJ, 112, 186
Kerr, R. M. P., Rizzuto, A. C., Kraus, A. L., & Offner, S. S. R. 2021, ApJ, 917, 23
Kipping, D. M. 2013, MNRAS, 435, 2152
Klein, B., Zicher, N., Kavanagh, R. D., et al. 2022, arXiv:2203.08190 [astro-ph]
Kolbl, R., Marcy, G. W., Isaacson, H., & Howard, A. W. 2015, AJ, 149, 18
Kollmeier, J. A., Zasowski, G., Rix, H.-W., et al. 2017, arXiv e-prints, arXiv:1711.03234
Kounkel, M., & Covey, K. 2019, AJ, 158, 122
Kraus, A. L., Ireland, M. J., Huber, D., Mann, A. W., & Dupuy, T. J. 2016, AJ, 152, 8
Kraus, A. L., Shkolnik, E. L., Allers, K. N., & Liu, M. C. 2014, AJ, 147, 146
Krumholz, M. R., McKee, C. F., & Bland-Hawthorn, J. 2019, ARA&A, 57, 227
Kuhn, M. A., Hillenbrand, L. A., Sills, A., Feigelson, E. D., & Getman, K. V. 2019, ApJ, 870, 32
Lallement, R., Babusiaux, C., Vergely, J. L., et al. 2019, A&A, 625, A135
Lallement, R., Capitanio, L., Ruiz-Dern, L., et al. 2018, A&A, 616, A132
Lee, E. J., & Connors, N. J. 2021, ApJ, 908, 32
Lopez, E. D., Fortney, J. J., & Miller, N. 2012, ApJ, 761, 59
Luger, R., Agol, E., Foreman-Mackey, D., et al. 2019, AJ, 157, 64
Mann, A. W., Newton, E. R., Rizzuto, A. C., et al. 2016, AJ, 152, 61
Mann, A. W., Gaidos, E., Vanderburg, A., et al. 2017, AJ, 153, 64
Mann, A. W., Wood, M. L., Schmidt, S. P., et al. 2022, AJ, 163, 156
Martioli, E., Hébrard, G., Correia, A. C. M., Laskar, J., & Lecavelier des Etangs, A. 2021, A&A, 649, A177
McInnes, L., Healy, J., & Astels, S. 2017, The Journal of Open Source Software, 2, 205
McQuillan, A., Mazeh, T., & Aigrain, S. 2014, ApJS, 211, 24
Meingast, S., Alves, J., & Fürnkranz, V. 2019, A&A, 622, L13
Meingast, S., Alves, J., & Rottensteiner, A. 2021, A&A, 645, A84
Morris, R. L., Twicken, J. D., Smith, J. C., et al. 2017, Kepler Science Document KSCI-19081-002
Morton, T. D. 2012, ApJ, 761, 6
Morton, T. D. 2015, VESPA: False positive probabilities calculator, Astrophysics Source Code Library, record ascl:1503.011
Morton, T. D., Bryson, S. T., Coughlin, J. L., et al. 2016, ApJ, 822, 86
Nardiello, D., Piotto, G., Deleuil, M., et al. 2020, MNRAS, 495, 4924
Newton, E. R., Mann, A. W., Tofflemire, B. M., et al. 2019, ApJ, 880, L17
Owen, J. E. 2020, MNRAS, 498, 5030
Owen, J. E., & Wu, Y. 2013, ApJ, 775, 105
—. 2017, ApJ, 847, 29
Pecaut, M. J., & Mamajek, E. E. 2016, MNRAS, 461, 794
Petigura, E. A., Howard, A. W., Marcy, G. W., et al. 2017, AJ, 154, 107
Petigura, E. A., Marcy, G. W., Winn, J. N., et al. 2018, AJ, 155, 89
Petigura, E. A., Rogers, J. G., Isaacson, H., et al. 2022, AJ, 163, 179
Plavchan, P., Barclay, T., Gagné, J., et al. 2020, Nature, 582, 497
Raghavan, D., McAlister, H. A., Henry, T. J., et al. 2010, ApJS, 190, 1
Randich, S., Tognelli, E., Jackson, R., et al. 2018, A&A, 612, A99
Rebull, L. M., Stauffer, J. R., Cody, A. M., et al. 2020
—. 2018, AJ, 155, 196
Rebull, L. M., Stauffer, J. R., Bouvier, J., et al. 2016, AJ, 152, 113
Ricker, G. R., Winn, J. N., Vanderspek, R., et al. 2015, JATIS, 1, 014003
Rizzuto, A. C., Newton, E. R., Mann, A. W., et al. 2020, AJ, 160, 33
Rogers, J. G., & Owen, J. E. 2021, MNRAS, 503, 1526
Röser, S., Schilbach, E., & Goldman, B. 2016, a, 595, A22
Salvatier, J., Wieckiâ, T. V., & Fonnesbeck, C. 2016, PyMC3: Python probabilistic programming framework
Schönrich, R., Binney, J., & Dehnen, W. 2010, MNRAS, 403, 1829
Short, C. I., & Doyle, J. G. 1998, a, 336, 613
Skumanich, A. 1972, ApJ, 171, 565
Smith, J. C., Morris, R. L., Jenkins, J. M., et al. 2016, PASP, 128, 124501
Smith, J. C., Stumpe, M. C., Jenkins, J. M., et al. 2017, Kepler Science Document, 8
Soderblom, D. R., Jones, B. F., Balachandran, S., et al. 1993, AJ, 106, 1059
Stephenson, C. B. 1959, PASP, 71, 145
Theano Development Team. 2016, arXiv e-prints, abs/1605.02688
Thompson, S. E., Coughlin, J. L., Hoffman, K., et al. 2018, ApJS, 235, 38
Tofflemire, B. M., Rizzuto, A. C., Newton, E. R., et al. 2021, AJ, 161, 171
Vogt, S. S., Allen, S. L., Bigelow, B. C., et al. 1994, SPIE Conference Series, ed. D. L. Crawford & E. R. Craine, Vol. 2198
Wright, N. J., & Mamajek, E. E. 2018, MNRAS, 476, 381
Yee, S. W., Petigura, E. A., & von Braun, K. 2017, ApJ, 836, 77

Zari, E., Hashemi, H., Brown, A. G. A., Jardine, K., & de Zeeuw, P. T. 2018, A&A, 620, A172

Zhao, G., Zhao, Y.-H., Chu, Y.-Q., Jing, Y.-P., & Deng, L.-C. 2012, Research in Astronomy and Astrophysics, 12, 723

Zhou, G., Quinn, S. N., Irwin, J., et al. 2021, AJ, 161, 2

Zicher, N., Barragán, O., Klein, B., et al. 2022, arXiv:2203.01750 [astro-ph]

Zieba, S., Zwintz, K., Kenworthy, M. A., & Kennedy, G. M. 2019, A&A, 625, L13

APPENDIX

A. CANDIDATE CEP-HER MEMBERS

Table 2 —contains candidate Cep-Her members with weights $D > 0.02$ observed by Kepler. The final catalog of candidate Cep-Her members will be provided by R. Kerr et al. in prep; Table 2 is from a preliminary version of that work. Note that more restrictive weight cuts should be imposed should one wish to remove the majority of field star interlopers; at least half of the stars included in the table are unlikely to be bonafide Cep-Her members. Table 2 was created by cross-matching candidate Cep-Her members (selected using Gaia EDR3; Section 2.2) against a Kepler to Gaia DR2 cross-match (the `gaia-kepler.fun` crossmatch database created by Megan Bedell). The `kic_dr2_ang_dist` column is from the latter table. The EDR3 to DR2 match was performed using the `gaiaedr3.dr2_neighbourhood` table, and the closest proper motion and epoch-corrected angular distance neighbor was taken as the single best match. The `edr3_dr2_mag_diff` column gives some indication of the reliability of this EDR3 to DR2 conversion, as there are a few cases between Gaia DR2 and EDR3 where partially resolved binaries became fully resolved.

Candidate matches between Cep-Her and the Kepler Objects of Interest: —The full list of candidate matches between Cep-Her and the Kepler objects of interest is as follows – the objects are listed in order of descending weights, D. Objects designated as confirmed planets included Kepler-1627, Kepler-1643, Kepler-1331, Kepler-1062, and Kepler-1933. Objects designated as candidate planets included KOI-5264, KOI-8007, KOI-7572, KOI-7375, KOI-7368, KOI-7638, KOI-5632, and KOI-7913. Objects designated known false positive planet candidates included KOI-6437, KOI-5988, KOI-7871, KOI-7655, KOI-5024, KOI-61, KOI-4336, KOI-6812, KOI-3399, and KOI-6277. Finally, Kepler-1902 (KOI-3090) has one confirmed planet (KOI-3090.02), and one false positive (KOI-3090.01). Of these objects, only Kepler-1627, Kepler-1643, KOI-7368, and KOI-7913 met our requirements for potentially both *i)* having real planets, and *ii)* being $\lesssim 10^8$ years old, based on the presence of rotational modulation at the expected period and amplitude. One object was ambiguous: Kepler-1933. This system has a confirmed $\approx 1.4\,R_\oplus$ planet, a stellar rotation period of 6.5 days, and an effective temperature of $\approx$5750 K. This places it near the upper envelope of the rotation period vs. color distribution for the Pleiades, making it unlikely to be $\approx$40 Myr old. Nonetheless, we acquired a reconnaissance HIRES spectrum, and it yielded $\mathrm{EW_{Li}} = 93 \pm 5$ mÅ. Combined with the rotation period, this suggests an age between 100 and 200 Myr for Kepler-1933, but the system is unlikely to be part of Cep-Her.

Table 3 —contains spatial, kinematic, astrometric, and rotation period information for the 173 candidate RSG-5 members and 37 candidate CH-2 members described in Section 2.2. These are the data used to make the lower panels of Figure 2; as with Table 2, these are from a preliminary version of the SPYGLASS 1 kpc expansion (R. Kerr et al. in prep). We adopted the ZTF period over the TESS period in three cases: (1) Gaia EDR3 2081755809272821248: the Lomb-Scargle periodogram favored 6.67 days, consistent with the ZTF period of 6.61 days; however, we flagged it as a candidate double-dipper, which appears to have inaccurately doubled the TESS period to 13.34 days; (2) Gaia EDR3 2081737529891330560: we found 3.06 days with TESS and 6.64 days with ZTF; we suspect that TESS captured the 1/2-period harmonic and adopt the approximately double value from ZTF; (3) 2134851775526125696: for this star, we measured 1.91 days with TESS from Cycle 2, but noted that the signal appeared to be missing in Cycle 4; ZTF found a strong signal at 12.23 days and we adopt this as the star's period. In the remaining overlap cases, we adopted the average between TESS and ZTF as the final period. For these overlap stars, the median absolute deviation is 0.01 days, showing remarkable consistency between the surveys. For three stars, we failed to detect a period in TESS but recovered one from ZTF; in all cases the periods appear to be 13–16 days. These stars were: (1) Gaia EDR3 2129930258400157440, for which TESS showed a flat light curve while ZTF yielded a 15.3-day period; (2) Gaia EDR3 2082376861542398336, LS found a 7.6-day period which we rejected during visual validation; we found 15.4 days with ZTF, and we suspect that the weak/rejected signal form TESS might have been a 1/2 period harmonic; (3) Gaia EDR3 2082397099429013120, similar to the previous case, we rejected a 6.7-day signal from TESS and recovered a 12.8-day period with ZTF.

B. SPECTROSCOPIC YOUTH INDICATORS

Figure 5 shows key portions of the HIRES and TRES spectra for the Kepler objects in Cep-Her. Lithium absorption is obvious at 6708Å in all stars except KOI-7913 B, where it is marginal. Hα is in emission for both components of KOI-7913, and in absorption for the hotter stars. In the following, we compare these observations against stars in benchmark open clusters.

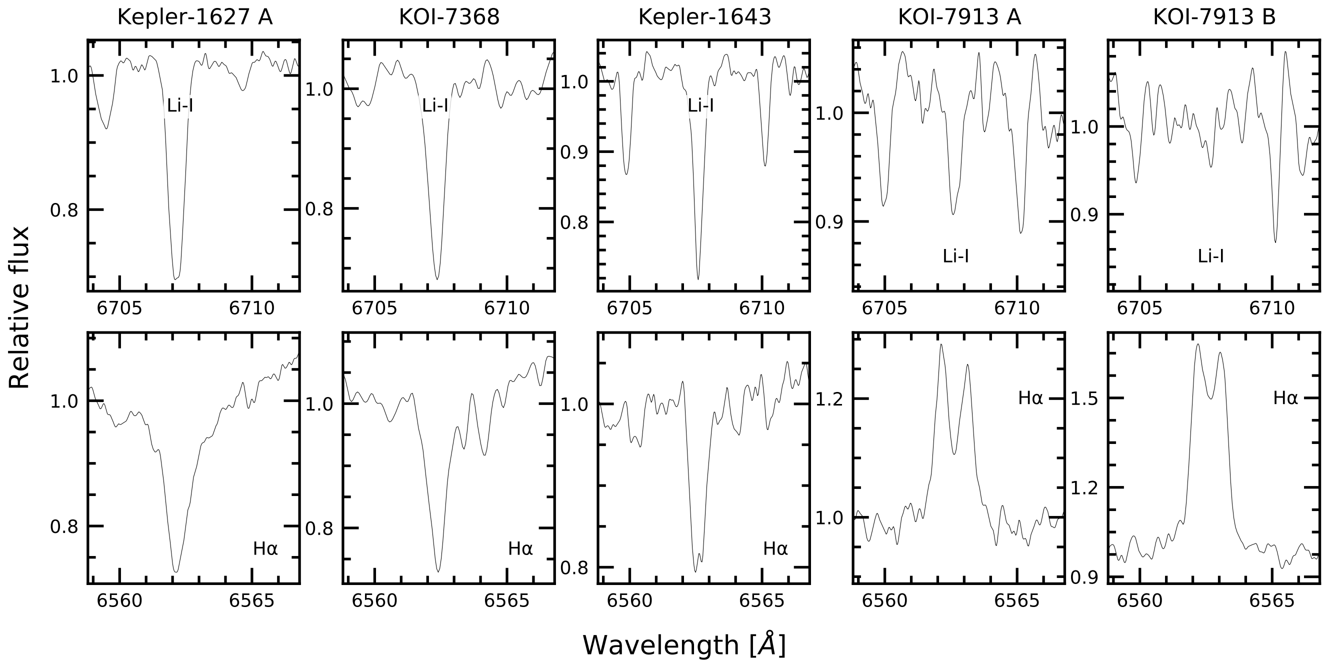

Figure 5. Spectroscopic youth diagnostics for Kepler-1627, KOI-7368, Kepler-1643, and KOI-7913 AB. The spectra are shown in the observed frame, and the stars are sorted left-to-right in order of decreasing effective temperature.

B.1. *Lithium*

Figure 6 compares the measured lithium equivalent widths of the Kepler objects against a few reference populations. We selected studies from the literature only where upper limits were explicitly reported. KOI-7368 and KOI-7913 A have secure lithium detections, while for KOI-7913 B the detection is marginal ($\mathrm{EW_{Li}} = 42^{+12}_{-19}$ mÅ). For all three stars, as well as for Kepler-1627 A, the observed lithium equivalent width is consistent with the stellar effective temperatures and ≈ 40 Myr ages.

Kepler-1643, in RSG-5, is conspicuously below the 40-50 Myr sequence in the left-panel of Figure 6, while still being above the field stars ($\mathrm{EW_{Li}} = 130^{+6}_{-5}$ mÅ). The right panel shows the comparison against the Pleiades, where Kepler-1643 is more consistent with the observed dispersion in lithium.

One explanation for this could be that Kepler-1643 is a field interloper; another could be that RSG-5 is much older than 50 Myr. We do not favor either, given that *i)* the star was selected based on its spatio-kinematic proximity to other RSG-5 members, nearly all of which appear consistent with being $\approx$50 Myr old (Figure 2 upper left), and *ii)* the same RSG-5 members display a gyrochronal sequence consistent with being younger than the Pleiades (Figure 2 lower left). There is a $\approx$1% chance of being a field interloper based on the spatio-kinematic selection, and a similar independent chance ($\approx$1%) of a field K2V star having a rotation period below the Pleiades (McQuillan et al. 2014). The extra observation of a strong lithium detection at these effective temperatures yields a very small probability for Kepler-1643 being a field interloper. It also seems unlikely that RSG-5 could be much older than 50 Myr, based on its proximity to the δ Lyr cluster and IC 2602 in the CAMD, as well as the data shown in rotation versus color diagram.

Our preferred explanation for Kepler-1643's lithium equivalent width is tied to the reference sample of IC 2602 and Tuc-Hor stars not fully exploring the possible stellar rotation periods and lithium equivalent widths. Analyzing Figure 6, it is remarkable that in just 50 million years, K-dwarfs between 4500 K and 5200 K go from having a tight lithium sequence to one with a dispersion $\approx 10\times$ greater. The existence of the Li dispersion in Pleiades-age K-dwarfs has been known for decades; it has also been known that the stars with the largest lithium abundances are also the most rapidly rotating (Butler et al. 1987; Soderblom et al. 1993). More recent analyses of this correlation have been reviewed by Bouvier (2020). The conclusion of that work was that the origin of the rotation-lithium correlation likely lies within pre-main-sequence stellar physics. If so, one would expect the IC 2602 and Tuc-Hor K-dwarfs to show a larger intrinsic lithium dispersion. A recent analysis of the $\approx$40 Myr NGC 2547 by Binks et al. (2022) suggests that this may be the case, though it only had $\approx$10 stars in the relevant effective temperature range.

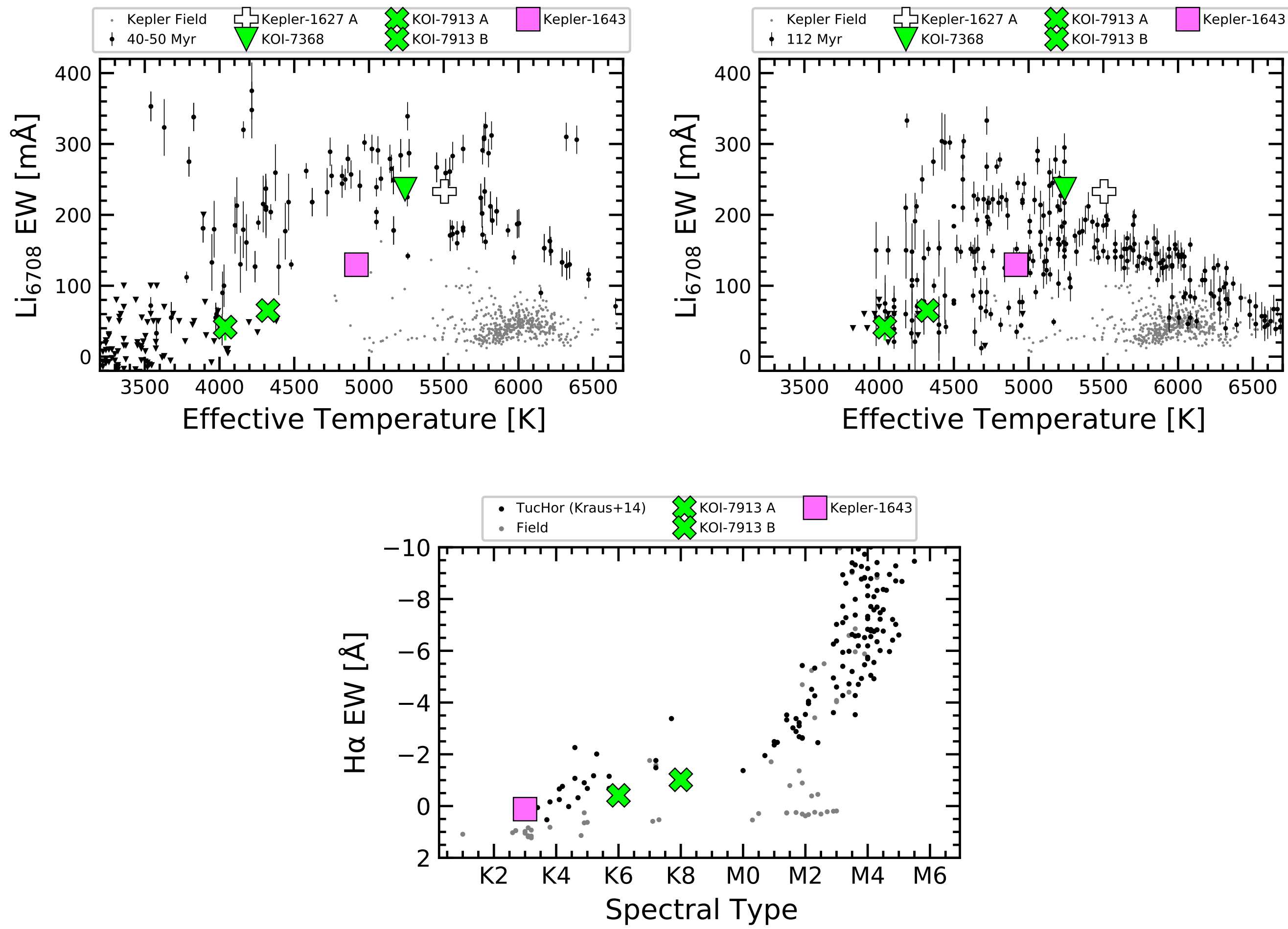

Figure 6. Lithium 6708Å and Hα equivalent widths for the objects of interest compared to young open clusters and field stars. Positive equivalent width means absorption; negative equivalent width means emission. The statistical uncertainties on the newly measured equivalent widths are shown, or else are smaller than the markers. *Top*: The field stars are stars with Kepler planets from Berger et al. (2018). The "40-50 Myr" reference stars (left) are from IC 2602 (Randich et al. 2018) and Tuc-Hor (Kraus et al. 2014). The "112 Myr" stars (right) are from the Pleiades (Soderblom et al. 1993; Jones et al. 1996; Bouvier et al. 2018). *Bottom*: The Hα comparison is against Tuc-Hor ($\approx$40 Myr; Kraus et al. 2014)

This suggests that RSG-5 and Cep-Her could be worthy objects for a closer analysis of the lithium-rotation correlation near the zero-age main sequence.

B.2. *Hα*

As shown in Figure 5, Hα is in emission for both components of KOI-7913, and in absorption for the hotter stars. Additionally, the emission appears double-peaked for both of the KOI-7913 components. An important note is that KOI-7913 A and KOI-7913 B were spatially resolved from each other during data acquisition. Performing a cross-correlation between each of the stars and the nearest matches in the Keck/HIRES template library, we also found that the CCFs for both components of KOI-7913 showed no indications of double-lined binarity (Kolbl et al. 2015).

Balmer line emission, particularly for Hα, is expected for stars of this age. Kraus et al. (2014) for instance, in their survey of Tuc-Hor ($\approx$40 Myr), observed that all cluster members with spectral type >K4.5V had Hα in emission. The agrees with our observations that KOI-7913 shows Hα in emission for both components, while it is in absorption for all of our other Kepler objects. The double-peaked nature of the emission, though not always present, is also common for active stars. Proxima Centauri, for instance, has double-peaked Hα emission (Collins et al. 2017). A simple explanation is self-absorption: photons nearest the center of the line see a greater optical depth from higher layers of the chromosphere, while photons on the wings are on average too far from the rest-wavelength to excite electrons and be re-absorbed in the upper layers. The exact details of when a star's atmosphere reaches the conditions for such self-absorption require non-local thermal equilibrium models of the chromosphere (Short & Doyle 1998; Fuhrmeister et al. 2005).

C. TABLE OF TRANSIT FIT PARAMETERS

Table 4 gives the full set of fitted and derived parameters from the model described in Section 4.2. Priors and convergence statistics are also listed.

D. DISPOSITION HISTORY OF KOI-7913

The disposition of KOI-7913.01 has been debated: in `q1_q17_dr25_koi` the source was flagged as a false positive, with the comment "cent_kic_pos—halo_ghost". This comment and disposition were removed in the `q1_q17_dr25_sup_koi` data release, which renamed the planet a "candidate". In this note, we discuss the interpretation of these flags (which do not apply to the system, according to the latest analysis). We also discuss how the relative on-sky positions of KOI-7913 A and KOI-7913 B affect the interpretation of the Kepler data.

As described by Thompson et al. (2018), the "cent_kic_pos" flag is an indication that the measured source centroid is offset from its expected location in the Kepler Input Catalog. The final Kepler data validation reports, generated 2016 Jan 30, do not show this to be the case for KOI-7913. Moreover, the statistical significance of any centroid offset is lower than for KOI-7368 and Kepler-1643 (which both show centroid offsets that are likely explained by the stellar variability).

What of the "halo_ghost" flag? This test measures the transit strength for the pixels inside the aperture, and compares it to that measured in the ring of pixels around said aperture (the "halo"). One usually expects the transit signal to be strongest in the central aperture, rather than the halo. Two types of false positive scenarios can change this and trigger the flag: the first is when optical ghosts from bright eclipsing binaries reflect off the CCD, and contaminate the target star. The second is when the PRF of nearby stars directly overlaps with the PRF of the target star (see Thompson et al. 2018, Section A.5.2). The most obvious explanation for KOI-7913 is the latter case, given that KOI-7913 B is ≈ 0.9 Kepler pixels away from Kepler-7913 A and so it usually part of the "halo". Due to the on-sky orientation of KOI-7913 A and KOI-7913 B, the default "optimal aperture" selected in quarters 3, 7, 11, and 15 in fact included both stars, while for the remaining quarters KOI-7913 B was excluded from the optimal aperture but was included as part of the halo (see pages 35 through 71 of the data validation reports.)

Given the orientation of the stars and the $\approx$1.5 pixel FWHM of the Kepler pixel response function, some blending between the two stars is present. The pointing geometries from quarters 3, 7, 11, and 15 however did not affect the observed transit depths, which is an indication that the crowding metric applied in the data products accurately correct the mean flux level (Morris et al. 2017). Analysis of the target-pixel data that was separately acquired for KOI-7913 B also reveals a different stellar rotation period, and no hint of the transit signal.

Table 2. Candidate Cep-Her members observed by Kepler

Parameter	Example Value	Description
`dr2_source_id`	2073765172933035008	Gaia DR2 source identifier.
`dr3_source_id`	2073765172933035008	Gaia (E)DR3 source identifier.
`kepid`	5641711	KIC identifier.
`ra`	297.4099	Gaia EDR3 right ascension [deg].
`dec`	40.8972	Gaia EDR3 declination [deg].
`weight`	0.0409	Strength of connectivity to other candidate cluster members.
`v_l`	-0.5061	Longitudinal galactic velocity [$\mathrm{km\,s^{-1}}$].
`v_b`	-8.2328	Latitudinal galactic velocity [$\mathrm{km\,s^{-1}}$].
`x_pc`	-8035.42	Galactocentric X position coordinate [pc].
`y_pc`	331.44	Galactocentric Y position coordinate [pc].
`z_pc`	65.32	Galactocentric Z position coordinate [pc].
`kic_dr2_ang_dist`	0.298	Separation between KIC and Gaia DR2 positions [arcsec].
`edr3_dr2_mag_diff`	0.002	G-band difference between EDR3 and DR2 source match [mag].

NOTE—Table 2 is published in its entirety in a machine-readable format. One entry is shown for guidance regarding form and content.

Table 3. Rotation periods and kinematics for candidate RSG-5 and CH-2 members.

Parameter	Example Value	Description
`dr3_source_id`	2127562009133684480	Gaia (E)DR3 source identifier.
`ra`	291.0231	Gaia EDR3 right ascension [deg].
`dec`	46.4384	Gaia EDR3 declination [deg].
`parallax`	3.7099	Gaia EDR3 parallax [milliarcsec].
`ruwe`	0.981	Gaia EDR3 renormalized unit weight error.
`weight`	0.0870	Strength of connectivity to other candidate cluster members.
`v_l`	2.7793	Longitudinal galactic velocity [$\mathrm{km\,s^{-1}}$].
`v_b`	-2.8675	Latitudinal galactic velocity [$\mathrm{km\,s^{-1}}$].
`x_pc`	-8068.52	Galactocentric X position coordinate [pc].
`y_pc`	255.96	Galactocentric Y position coordinate [pc].
`z_pc`	86.25	Galactocentric Z position coordinate [pc].
`(BP-RP)0`	-0.115	Gaia $G_{\rm BP}$-$G_{\rm RP}$ color, minus $E(G_{\rm BP}$-$G_{\rm RP})$.
`(M_G)0`	0.442	Absolute G-band magnitude, corrected for extinction.
`cluster`	CH-2	RSG-5 or CH-2.
`Prot_Adopted`	NaN	Adopted rotation period [days].
`Prot_TESS`	NaN	TESS rotation period [days].
`Prot_ZTF`	NaN	ZTF rotation period [days].
`Prot_Confused`	NaN	Boolean flag; true when stars are photometrically blended.

NOTE—Table 3 is published in its entirety in a machine-readable format. One entry is shown for guidance regarding form and content.

Table 4. Priors and posteriors for the transit models with local polynomials removed.

Param.	Unit	Prior	Median	Mean	Std. Dev.	3% HDI	97% HDI	ESS	$\hat{R}-1$
				Kepler-1643					
P	d	$\mathcal{N}(5.34264; 0.01000)$	5.3426257	5.3426258	0.0000101	5.3426071	5.3426454	7884	1.1e-03
$t_0^{(1)}$	d	$\mathcal{N}(134.38100; 0.02000)$	134.3820412	134.3820408	0.0011172	134.3798834	134.3840798	7390	3.7e-04
$\log R_\mathrm{p}/R_\star$	–	$\mathcal{U}(-6.215; 0.000)$	-3.68806	-3.68934	0.02072	-3.72788	-3.65275	4449	-7.8e-05
b	–	$\mathcal{U}(0; 1+R_\mathrm{p}/R_\star)$	0.5825	0.5781	0.0514	0.4848	0.6734	4705	1.9e-04
u_1	–	Kipping 2013	0.257	0.294	0.214	0.000	0.678	5324	7.9e-04
u_2	–	Kipping 2013	0.324	0.314	0.324	-0.257	0.880	4908	8.4e-04
$R_\star$	$R_\odot$	$\mathcal{N}(0.855; 0.044)$	0.851	0.851	0.045	0.766	0.933	7473	7.2e-04
$\log g$	cgs	$\mathcal{N}(4.502; 0.035)$	4.507	4.507	0.035	4.442	4.576	6530	-1.4e-04
$\log \sigma_f$	–	$\mathcal{N}(\log\langle\sigma_f\rangle; 2.000)$	-8.520	-8.520	0.019	-8.556	-8.486	7966	2.1e-04
$\langle f \rangle$	–	$\mathcal{N}(1.000; 0.100)$	1.0000	1.0000	0.0000	1.0000	1.0000	7488	3.2e-04
$R_\mathrm{p}/R_\star$	–	–	0.025	0.025	0.001	0.024	0.026	4449	-7.8e-05
$\rho_\star$	g cm^{-3}	–	1.943	1.953	0.191	1.603	2.313	6081	9.4e-05
R_p	R_Jup	–	0.207	0.207	0.012	0.184	0.231	6326	2.5e-04
R_p	R_Earth	–	2.32	2.32	0.135	2.062	2.589	6326	2.5e-04
$a/R_\star$	–	–	14.312	14.322	0.465	13.487	15.228	6081	8.2e-05
$\cos i$	–	–	0.041	0.040	0.005	0.032	0.049	4929	2.4e-04
T_{14}	hr	–	2.408	2.409	0.061	2.304	2.527	4774	5.3e-04
T_{13}	hr	–	2.232	2.233	0.070	2.109	2.362	4561	6.2e-04
				KOI-7368					
P	d	$\mathcal{N}(6.84294; 0.01000)$	6.8430344	6.8430341	0.0000125	6.8430107	6.8430574	10045	6.5e-05
$t_0^{(1)}$	d	$\mathcal{N}(137.06000; 0.02000)$	137.0463023	137.0463315	0.0014043	137.0436532	137.0489229	10303	9.2e-05
$\log R_\mathrm{p}/R_\star$	–	$\mathcal{U}(-4.605; 0.000)$	-3.76025	-3.76299	0.03062	-3.81932	-3.70774	4043	6.3e-04
b	–	$\mathcal{U}(0; 1+R_\mathrm{p}/R_\star)$	0.5077	0.4999	0.0641	0.3797	0.6115	4434	3.5e-04
u_1	–	Kipping 2013	0.976	0.953	0.267	0.425	1.422	5809	-5.6e-05
u_2	–	Kipping 2013	-0.191	-0.158	0.308	-0.661	0.421	4387	2.6e-04
$R_\star$	$R_\odot$	$\mathcal{N}(0.876; 0.035)$	0.874	0.874	0.036	0.804	0.938	9902	7.3e-04
$\log g$	cgs	$\mathcal{N}(4.499; 0.030)$	4.503	4.502	0.030	4.445	4.557	7527	2.7e-05
$\log \sigma_f$	–	$\mathcal{N}(\log\langle\sigma_f\rangle; 2.000)$	-8.314	-8.314	0.012	-8.337	-8.292	10636	1.3e-03
$\langle f \rangle$	–	$\mathcal{N}(1.000; 0.100)$	1.0000	1.0000	0.0000	1.0000	1.0000	9742	-2.9e-04
$R_\mathrm{p}/R_\star$	–	–	0.023	0.023	0.001	0.022	0.025	4043	6.3e-04
$\rho_\star$	g cm^{-3}	–	1.872	1.878	0.151	1.593	2.159	6829	3.4e-04
R_p	R_Jup	–	0.198	0.198	0.011	0.177	0.218	5676	2.8e-04
R_p	R_Earth	–	2.219	2.219	0.123	1.984	2.444	5676	2.8e-04
$a/R_\star$	–	–	16.671	16.677	0.447	15.863	17.542	6829	3.3e-04
$\cos i$	–	–	0.030	0.030	0.004	0.022	0.038	4518	5.4e-04
T_{14}	hr	–	2.789	2.792	0.075	2.651	2.928	4845	5.0e-04
T_{13}	hr	–	2.619	2.622	0.085	2.470	2.779	4575	3.1e-04
				KOI-7913					
P	d	$\mathcal{N}(24.27838; 0.01000)$	24.2785532	24.2785706	0.0002630	24.2781117	24.2790852	4413	1.5e-03
$t_0^{(1)}$	d	$\mathcal{N}(154.51300; 0.05000)$	154.5121202	154.5124405	0.0062825	154.4998424	154.5237474	5612	6.0e-04
$\log R_\mathrm{p}/R_\star$	–	$\mathcal{U}(-5.298; 0.000)$	-3.59884	-3.60184	0.04605	-3.68852	-3.51878	4290	5.6e-04
b	–	$\mathcal{U}(0; 1+R_\mathrm{p}/R_\star)$	0.3120	0.2985	0.1526	0.0045	0.5232	2373	1.8e-03
u_1	–	Kipping 2013	0.267	0.337	0.281	0.000	0.862	4491	-6.1e-05
u_2	–	Kipping 2013	0.209	0.229	0.325	-0.309	0.860	5935	7.0e-04
$R_\star$	$R_\odot$	$\mathcal{N}(0.790; 0.049)$	0.788	0.788	0.049	0.699	0.881	6847	2.8e-04
$\log g$	cgs	$\mathcal{N}(4.523; 0.043)$	4.526	4.527	0.042	4.450	4.606	5714	6.6e-04
$\log \sigma_f$	–	$\mathcal{N}(\log\langle\sigma_f\rangle; 2.000)$	-7.197	-7.197	0.019	-7.230	-7.161	6976	1.4e-04
$\langle f \rangle$	–	$\mathcal{N}(1.000; 0.100)$	1.0000	1.0000	0.0000	1.0000	1.0000	6998	2.8e-04
$R_\mathrm{p}/R_\star$	–	–	0.027	0.027	0.001	0.025	0.030	4290	5.6e-04
$\rho_\star$	g cm^{-3}	–	2.199	2.213	0.250	1.781	2.705	5357	5.6e-04
R_p	R_Jup	–	0.209	0.209	0.016	0.179	0.238	4882	1.3e-03
R_p	R_Earth	–	2.343	2.343	0.179	2.006	2.668	4882	1.3e-03
$a/R_\star$	–	–	40.920	40.949	1.539	38.143	43.845	5357	6.6e-04
$\cos i$	–	–	0.008	0.007	0.004	0.000	0.013	2344	1.9e-03
T_{14}	hr	–	4.394	4.396	0.207	3.980	4.758	3952	5.6e-04
T_{13}	hr	–	4.133	4.132	0.222	3.715	4.548	3632	7.6e-04

NOTE— ESS refers to the number of effective samples. $\hat{R}$ is the Gelman-Rubin convergence diagnostic. Logarithms in this table are base-e. $\mathcal{U}$ denotes a uniform distribution, and $\mathcal{N}$ a normal distribution. Many of the T_{13} statistics may be `nan` in the event of a grazing transit. (1) The ephemeris is in units of BJKD (BJDTDB-2454833).